

DECLARATION

I hereby declare that this thesis is my original work and it has been written by me in its entirety. I have duly acknowledged all the sources of information which have been used in the thesis.

This thesis has also not been submitted for any degree in any university previously.

Len Yink Loong

9 January 2014

**Entanglement Detection With Minimal Tomography
Using Witness Bases Measurement**

Len Yink Loong
(*BSc. (Hons.)*, NUS)

Supervisor: Prof. Berthold-Georg Englert

A THESIS SUBMITTED
FOR THE DEGREE OF MASTER OF SCIENCE
DEPARTMENT OF PHYSICS
NATIONAL UNIVERSITY OF SINGAPORE

2014

Preface and Acknowledgments

This master thesis summarizes the two-year research I conducted as a research assistant (RA) of Professor Englert. More specifically, it summarizes mainly the experimental effort in detection of entanglement with entanglement witnesses, for photonic systems. As is usually the case in experimental physics, this project is not an individual effort. It is done together with a PhD. student, Jibo Dai of Centre for Quantum Technologies (CQT), in which this work is inclusive as part of his whole PhD project. On the other hand, this project is jointly supervised by Dr. Leonid Krivitsky from Data Storage Institute (DSI), where the laboratory is actually situated. As we started with little knowledge and skills in theoretical and experimental quantum optics, this project is a real challenge. Only with the valuable guidance, clarifications, assistances and support that we received from various people, this work is made possible.

Among them, I must first express my gratitude to my supervisor, Prof. Berthold-Georg Englert. Without his generous financial support through an offer for a RA position in CQT, there is no way I can bear the cost for my graduate studies in NUS. In addition, I am sincerely thankful for his academic guidance since my undergraduate studies, and for giving me the opportunity to explore the continuum of experimental physics during my Master's degree studies. Despite not being an experimentalist himself, he constantly provides feedback to us during discussions, helping us numerously on theoretical issues, and suggesting ideas for the experiment.

This project is impossible to carry on without Leonid's guidance on all the experimental aspects, including his courtesy in providing us the laboratory and the

apparatus required. He is very approachable for discussions and is very helpful. He has also been very patient in teaching us the relevant knowledge and skills, particularly as we are learning experimental optics from scratch.

Thirdly, I would like to thank my partner, Jibo, for sharing the work with me and always giving his best at it. He is definitely a good partner: He readily corrects my mistakes and misunderstandings on the subject, and covers up my inefficiencies. In addition, Dr. Yong Siah Teo helps us tremendously in processing the experiment data, particularly with his efforts in providing computational codes and performing numerical calculations. I sincerely thank him here.

Last but not least, I would like to extend my appreciation to the members in Berge's group at CQT and of Leonid's at DSI, my friends, professors at the Department of Physics, and my family: They all have been helpful and supportive at various stages towards the completion of this project, in one way or another. Thank you.

Contents

List of Figures	VII
List of Tables	XIII
Abstract & Summary	XV
I Theory	1
1 Background Concepts I	3
1.1 Quantum states: A brief review	3
1.1.1 Pure states	3
1.1.2 Mixed states	4
1.2 POM and quantum state tomography	5
1.2.1 POM	5
1.2.2 Quantum state estimation	7
1.3 Witnesses and entanglement quantification	9
1.3.1 Witness operator	10
1.3.2 Quantification of entanglement	10
2 Background Concepts II	15
2.1 Principles of entanglement detection	15
2.1.1 Detection of entanglement by witness basis	16
2.1.2 Witness bases as IC POM	17
2.1.3 Adaptive schemes	19
2.2 Photon polarization as qubit	20

2.2.1	Source of biphoton: SPDC	20
2.2.2	Polarization manipulations using optical devices	24
2.3	Realization of a witness-basis measurement	25
2.3.1	Hong-Ou-Mandel interferometer as witness basis	25
2.3.2	Change of witness basis to form POM	28
II	Experiment	29
3	Witness-Family Measurements	31
3.1	Generation of two-photon states	31
3.1.1	Bell states	32
3.1.2	Rank-1 states	33
3.1.3	Rank-2 states	34
3.2	Manipulations and control of states	36
3.2.1	Manipulation & control	36
3.2.2	HOM interferometer	36
3.3	Detection and measurement	38
3.3.1	Witness-basis measurement	38
3.3.2	Polarization correlation test	40
3.3.3	Characterization of HOM interferometer	41
3.3.4	Detector calibration	43
3.4	Rank-4 states	44
3.4.1	Expected statistics	45
3.4.2	Generating Werner states	46
3.4.3	Link to witness-basis measurement	47
3.5	A discussion: How the experiment is actually performed	48
4	Results	51
4.1	Fidelities	51
4.1.1	Rank-1 states	51
4.1.2	Rank-2 states	53
4.1.3	Rank-4 states	54
4.2	Simulation results	56

4.3	Experimental results	57
4.4	Statistical analysis: Bootstrapping	59
Conclusion		63
III	Appendix	65
A	Witness Basis	A-1
B	Birefringence and Phase Matching	B-1
C	Coherence Length and the Migdall Effect	C-1
D	SPDC Coupling and Polarization Control	D-1
	Bibliography	XI

List of Figures

1.1	Geometry of states and entanglement witnesses.	11
2.1	Non-collinear degenerate SPDC: A two-dimensional illustration. Inside the BBO crystal, the pump photon is spontaneously down-converted into signal and idler photons of degenerate wavelength. The crystal's optic axis and the pump's polarization are both in the plane of the page, making the pump an extraordinary ray. The signal and idler have polarizations perpendicular to the page, i.e. they are ordinary rays. This is known as Type-I phase matching, or 'e → o+o' configuration. In reality, there is a rotational symmetry around the axis of \mathbf{k}_p , so SPDC is observed as rings in three-dimensional space, where φ is called the <i>cone-opening angle</i>	22
2.2	<i>NIST Phasematch</i> software: By choosing the appropriate subjects or functions from the database, as shown in the picture are Type-I phase matching using BBO crystal, and inserting relevant values such as the crystal's thickness (800 μm), the pump's wavelength (404.6 nm), its full width at half maximum (0.6 mm) and the phase-matching angle θ (29.6°), the intensity spectra of the down-converted light as a function of wavelength and cone-opening angle φ can be obtained. As can be seen from the image, with the optic axis cut at 29.6°, most of the down-converted light emerged at an angle $\varphi \approx 4^\circ$	23

- 2.3 Realization of a witness-basis measurement using HOM interferences, with the signatures given in the Table 2.2. As an example, when the detectors at LH and LV ports both register photons simultaneously, this corresponds to a measurement signature for the $|\Phi^+\rangle$ eigenket. The wave plates WPs are used to change the witness basis for subsequent measurements, see Sec. 2.3.2. 27
- 3.1 Schematic for the generation of the Bell states and rank-1 states. A CW diode laser pumps two type-I BBO crystals with optic axes on orthogonal planes, and the SPDC occurs in the non-collinear frequency-degenerate regime. When the HWP is set at 22.5° , it changes the vertically polarized pump photons to -45° , and thereby produces the Bell states. To generate the class of rank-1 states given in Eq. (3.2), the HWP is set at ϑ . quartz plates (QP) are used to control the relative phase between the generated states from the two crystals. 32
- 3.2 Schematic for the generation of rank-2 states. A variable polarization rotator (VPR) is added to the Bell state generation set-up, so that the pump periodically changes between the $+45^\circ$ and -45° polarizations with controlled ratio. 34
- 3.3 From its source, the signal and idlers are collected into SMFs, using lenses (L). Their polarizations are maintained by using the PCs. The photons are directed to interfere at the 50:50 BS, and guided to incident on two PBSs. The IFs are interference filters. Set of wave plates are installed on both arms to perform changes of witness basis. To distinguish the signatures of the four eigenkets of the witness bases, eight detectors are used, and the coincidences between any two detectors are (post-)processed by a coincidence programme \otimes 37

- 3.4 An excerpt from the real experimental data for witness basis 1 with the $|\text{HH}\rangle$ ket, where $\vartheta = 90^\circ$ in Eq. (3.2). The left column is the timestamp, where one unit, or *time bin*, corresponds to 81 ps. The time window of 5 ns is then approximated by 62 bins. The right column is the channel number, which corresponds to the detectors shown in Fig. 3.3. Here, we have the mapping of channel numbers to detectors by $0 \leftrightarrow \text{D1}, 1 \leftrightarrow \text{D2}$, and so on. As an example, there is a coincidence count between D5 and D6 as highlighted above. In our experiments, there are about ten thousand such coincidence counts for each state and each witness basis. 39
- 3.5 Schematic of the experimental set-up for polarization correlation test. Using HWPs and PBSs, polarization correlation tests are performed in two bases, namely the HV basis and $\pm 45^\circ$ basis. D1 and D2 are single-photon detectors, and \otimes is the coincidence circuit. 40
- 3.6 Polarization correlation analyses, for the Bell ket $|\Psi^+\rangle$. The tests show strong polarization correlation between the down-converted photons which is independent of the measurement basis, and hence a confirmation of the highly-entangled source. Not shown are the single counts of the two detectors, which are both about 22,000 counts per ten seconds, and are almost not modulated by θ 41
- 3.7 The HOM dip. The stage position at around $130 \mu\text{m}$ indicates almost equal detection time for the photons, making them indistinguishable in principle. A sharp decrease in the coincidence rates is thus observed, as the stage translates along. The smooth curve is a fitted Gaussian, which corresponds to interference filters with Gaussian profile. 42
- 3.8 The coincidence counts at the HOM dip for ten minutes, both with cover (red), and without cover (black). To observe the instability more clearly, the above results were obtained without interference filters. Here, the maximum coincidence rates N_{max} is around 2000 counts per second. 43

4.1	Plot of tangle of the ML estimators, compared with the theoretical curve given by Eq. (3.3). The error bars are smaller than the symbols used.	52
4.2	Plots of tangle and purity of the ML estimators, compared with the theoretical curves given by Eq. (3.6) and Eq. (3.5) respectively. The error bars are smaller than the symbols used.	54
4.3	Plots of tangle and purity of the ML estimators, compared with the theoretical curves given by Eq. (3.13) and Eq. (3.12) respectively. The error bars are smaller than the symbols used.	55
4.4	Cumulative histograms showing the number of witnesses needed to detect 10,000 states, using various schemes proposed in Sec. 2.1 As a general trend, scheme C gives the best performance, followed by scheme B and A. Note that scheme C not only reduces the average witnesses needed, but it also increases the number of states detectable without performing quantum state tomography.	56
4.5	Histograms of percentage of states detected versus the number of witnesses needed. For both simulations (unshaded) and experimental (shaded) results, the number of states are about 10,000. The first row, i.e. (a) and (d), shows the results for rank-1 states. Similarly, the second and third row show the results for rank-2 and rank-4 states respectively. The first column, i.e. histograms (a), (b) and (c) summarizes the results obtained by using scheme B, while the second column summarizes the results with scheme C. The high fidelities ($\approx 99\%$) of the histograms show that the experimental and simulation results agree very well.	58

- 4.6 Histograms for simulated (unshaded), and experimental (shaded) results, with error bars added using the technique of bootstrapping. The first and second rows are histograms for rank-1 and rank-2 states respectively; the first and second columns are histograms for scheme B and scheme C respectively. Here, both the error bars for the simulation and bootstrap histograms are derived from 100 ensembles of about 10,000 qubit copies. The attached error bars represent one standard deviation of the number of witnesses needed. From the histograms, we see clearly that the error bars for both simulation and experimental results are very similar in size. The average fidelities are also high ($\approx 95\%$). 61
- D.1 Illustration of how the lens captures the SPDC photons at d distance away, and couples them into the single mode with NA=0.12, located at its focus. D-2

List of Tables

2.1	The six witnesses that collectively form an IC POM, and the unitary operators relating them.	18
2.2	Signatures of eigenkets of the witness operators.	27
3.1	Signatures of measuring the eigenkets of witness operators, using the configuration in Fig. 3.3.	38
4.1	Rank-1 states: Fidelities of the ML estimators with the target states given by Eq. (4.1) are computed. The tangles of the ML estimators are also compared with the expected value of Eq. (3.3). The purity of the ML estimators are also included; theoretically, they should be one.	52
4.2	Rank-2 states: Fidelities of the ML estimators with the target states given by Eq. (4.2) are computed. The tangles of the ML estimators (Ep) are also compared with the expected value of Eq. (3.6) (Th). The purities of the ML estimators are also included; they are to be compared with Eq. (3.5).	53
4.3	Rank-4 states: Fidelities of the ML estimators with the target states given by Eq. (4.3) are computed. The tangle of the ML estimators (Ep) are also compared with the expected value of Eq. (3.13) (Th). The purity of the ML estimators are also included; they are to be compared with Eq. (3.12). The last two states are not used for testing the witness-family measurements.	55

- 4.4 Average number of witnesses needed (with standard deviations) to detect entanglement for rank-1 and rank-2 states by using scheme B and scheme C respectively. In general, scheme C has a smaller mean number of witnesses needed, as well as a smaller spread. 62

Abstract and Summary

- How many witnesses do we have to measure to determine whether a generic unknown quantum state is *entangled* or not?

This question is answered by Zhu *et. al.* [ZTE10]:

- As many as the dimension d of the state space: By measuring a set of witness operators which collectively form an informationally complete (IC) probability operator measurement (POM).

It is well known that by utilizing the very definition of witness operators, one might be able to directly detect entanglement without necessarily knowing what the identity of the state. If one is lucky, then one such witness measurement will do. However, in general, infinitely many witness measurements are needed, if one ignores the detailed information that each measurement provides. In contrast, with all the witness measurements taken collectively as an IC POM, although one might not be able to detect entanglement from these individual measurements, one can still reconstruct the state using various tomographic techniques. With the reconstructed state at hand, identification of entanglement is then straightforward. While designing experiments for high dimensional quantum states is a difficult subject,

- for *bipartite qubit* photonic systems, one can realize the measurement of the witness operators readily, using existing linear-optics devices. In fact, Zhu *et. al.* [ZTE10] had described an elegant scheme for such an experiment: By systematically measuring the *eigenbases* of the witnesses, one can further simplify the problem to measuring only six witness *families* for this particular state space of 16 dimensions.

The main objective of this project is straightforward:

- Based on the proposed scheme, we carry out the witness-family experiments, and eventually verify an efficient method for entanglement detection.

That is, we build up an experimental set-up that performs the witness-family measurements, such that by investigating and analyzing the results obtained from using various states with *known* degrees of entanglement, the validity of the scheme shall be tested and verified.

This thesis summarizes the effort in pursuing our goal to verify an efficient scheme for detecting entanglement. The organization of this thesis is as follow: In Part I, essential theoretical concepts of relevance are firstly reviewed. In the first chapter, a brief recap of some basic concepts of the characterization and detection of quantum states are presented. Readers who are familiar with concepts like POM, quantum state tomography, witnesses, and etc., may skip Chapter 1 and proceed to Chapter 2. In Chapter 2, we address the principles of entanglement identification and its realization in our experiment, where in going beyond the original experimental proposal, adaptive schemes are introduced to further speed up the entanglement detection. Related topics about the quantum resources used, i.e. photons and their polarizations, are also discussed.

In Part II, we report our experimental effort. In Chapter 3, the actual implementation of the witness-family measurements is presented in full details. We also summarize the effort in generation of various states which are used as test sources for the entanglement-detection scheme. To highlight, we introduced a novel, controllable and simple way of generating mixed two-photon states with various degrees of entanglement, with the help of variable polarization rotators. This work has been published in June 2013 in *New Journal of Physics* [DLT⁺13], with the arxiv preprint version available at <http://arxiv.org/abs/1304.2101>. In Chapter 4, the findings of our experiment are reported. Results, data analyses and discussions are presented in detail. As of now (April 29, 2014), a manuscript reporting our findings is submitted to a peer-reviewed journal for publication; an arxiv preprint of the manuscript is available at <http://arxiv.org/abs/1402.5710>.

Lastly, we conclude the findings of our project, and appendices are attached for more detailed discussions on selected topics.

Part I

Theory

Chapter 1

Background Concepts I

This chapter serves to recall some relevant preliminary concepts, namely on the studies of quantum states.

1.1 Quantum states: A brief review

1.1.1 Pure states

In quantum theory, the optimal knowledge or description of a basic quantum system is symbolized by the *state vector*, usually denoted as $|\ \rangle$ (or $\langle \ |$), called the Dirac's *ket* (or *bra*). For example, a ket $|\text{H}\rangle$ symbolizes a photon with horizontal polarization. In addition, the sets of kets and bras form Hilbert spaces of dimension D that are dual to each other¹. Introducing an orthonormal basis, say $\{|k\rangle\}_{k=1,2,\dots,D}$ for the ket space of dimension D , the inner product $\text{tr}\{|\ \rangle\langle k|\} = \langle k|\ \rangle$ represents the overlap of $|\ \rangle$ with $|k\rangle$, which is in general a complex number with a magnitude normalized to not greater than unity. Thus, one can write

$$|\ \rangle = \sum_{k=1}^D |k\rangle\langle k|\ \rangle, \quad (1.1)$$

which expresses a ket in terms of a chosen basis. In the example of photon polarization, the dimension of the Hilbert space is two, since any polarization can be decomposed into linear combination of two independent ones. Such a system of

¹Formally, Hilbert spaces are infinite-dimensional vector spaces. Taking it for granted, we shall include (and hereafter, focus only on) finite-dimensional vector spaces as Hilbert spaces.

two-dimensional Hilbert space is called a *qubit*, and the most popular orthogonal basis is perhaps $\{|H\rangle, |V\rangle\}$, where $|V\rangle$ represents vertical polarization.

For a system composed of two subsystems, called a *bipartite system*, the extension of symbols for states is straightforward, with the tensor product \otimes between the two subsystems' states. For instance, $|H\rangle_A \otimes |H\rangle_B$, or simply $|HH\rangle$, identifies a pair of horizontally polarized photons from subsystems A and B. Immediately, one can anticipate legitimate states with no classical description through the superposition of such *product states*: Consider the singlet Bell ket, $|\Phi^-\rangle = \frac{1}{\sqrt{2}}(|HV\rangle - |VH\rangle)$, which says that if one photon is determined as horizontally polarized, it will be vertical for the other. This characteristic of having correlated polarizations persists, even if the measurement was done in any other orthogonal basis. That is, we obtain less information about the photons as individuals, but gain in knowledge about them as a pair. This kind of intimate *quantum correlation* between two subsystems, which is non-classical in nature, is known as *entanglement*. More precisely, for a k -partite system, one calls the ket entangled if it is a superposition ket, which cannot be factorized completely into tensor products of kets of all individual subsystems.

1.1.2 Mixed states

It is evident that more generally, the ket or bra notation alone is not sufficient to describe all quantum systems accurately. For instance, we might have situation such as the system is in thermal equilibrium with the environment, or more generally, we might find the need to deal with an *ensemble* of systems, instead of just one. Such a generic ensemble could consist of purely identical copies of a quantum system, or *mixtures* of different ones. The generalization of the ket/bra is the *statistical operator*, ρ , which allows description of broader classes of physical systems. Another common and well-accepted terminology for the statistical operator is the “*state*”. Then, the first kind of ensemble above is known as *pure states*, and the second kind as *mixed states*.

The generic form of statistical operator is $\rho = \sum_i |i\rangle g_i \langle i|$, where $|i\rangle$ is the ket of the i -th type system, and g_i is its weight in the mixture. Note that this decomposition is generally not unique: There are infinitely many *as-if realities* for a given state,

with pure states being the exception. Then, the generalization of entanglement are as follows:

- States which can be written as $\rho = \sum_i g_i \rho_{1,i} \otimes \rho_{2,i} \cdots \otimes \rho_{k,i}$ are known as *separable*,
- states which are not separable are (fully) *entangled*.

Physically speaking, a separable state describes a mixture of systems which can be obtained by preparing all individual subsystems of the k -partite separately and in well-defined states. In other words, all the subsystems retain their individuality, and have no quantum correlations with each other.

Two remarks are in order: First, we refer the dimension d of the *state space* (the space of all statistical operators) as the number of entries of the *density matrix*, i.e. the representation of statistical operator in any basis. For example, bipartite qubit systems have a $d=16$ -dimensional state space. Secondly, we call states with n non-zero eigenvalues as *rank- n* states. For instance, pure states are rank-1 states, mixtures of two orthogonal pure states are rank-2 states.

Purity

A simple measure of mixedness of the state ρ is given by its *purity*, $P = \text{tr}\{\rho^2\}$. The values of the purity are bounded between $1/\sqrt{d}$ and one. It equals to one if and only if ρ is pure, and equals to $1/\sqrt{d}$ when ρ is *completely mixed*, i.e. $\rho = \mathbb{1}/\sqrt{d}$, where $\mathbb{1}$ is the identity operator. Obviously, the completely mixed state is a rank- \sqrt{d} state.

1.2 POM and quantum state tomography

1.2.1 POM

We now review the subject of measurement in quantum mechanics. As measurements are operations acting on the system, they are represented by measurement operators M_a , with a labeling the outcomes of the measurement. Regardless of the details of the measurement, such as the exact physical nature of the measurement, or the state of the system after the measurement, a consistent measurement theory must satisfy the following two criteria:

- The probability of occurrence, p_a , for the outcome of measurement operator M_a must be non-negative,
- the probabilities for all outcomes are summed to unity, assuming no losses.

We remark that the probabilistic nature of measurement outcomes is inherent in quantum phenomena. To proceed, following Schwinger [Sch00, Sch01], we can think of the act of measurement as a two-step process: First we annihilate selectively, followed by re-creation, or update, of the quantum system into a new state. That is, a unit prototype for selective measurement operator looks like

$$M_a = |a\rangle\langle b|, \quad (1.2)$$

such that when applied on the state $|\rangle$, the outcome is the new state $|a\rangle$, happened with a probability that is proportional to the overlap $\langle b| \rangle$. It is evident that only the annihilation or selection stage should matter for the probability of the outcome, and hence we anticipate that

$$0 \leq p_a = \text{pr}\{M_a, |\rangle\} = \text{pr}\{|a\rangle\langle b|, |\rangle\} = f(\langle b|, |\rangle) = f(\langle b| \rangle) \leq 1. \quad (1.3)$$

The function f can be determined from considering first the special case of *projective measurement*, in which $M_a = |a\rangle\langle a|$, and $\langle a|a'\rangle = \delta(a, a')$. Together with Eq. (1.1),

$$\sum_a p_a = 1 = \langle |\rangle = \sum_a \langle |a\rangle\langle a| \rangle = \sum_a \left| \langle a| \rangle \right|^2, \quad (1.4)$$

identifying $f(x) = |x|^2$. This generalizes to

$$p_a = \left| \langle b| \rangle \right|^2 = \langle \underbrace{|b\rangle\langle a|}_{M_a^\dagger} \underbrace{|a\rangle\langle b|}_{M_a} \rangle = \langle |M_a^\dagger M_a| \rangle = \text{tr}\{M_a| \rangle \langle M_a^\dagger\}, \quad (1.5)$$

and thus,

$$p_a = \text{tr}\{M_a \rho M_a^\dagger\} = \text{tr}\{M_a^\dagger M_a \rho\}. \quad (1.6)$$

Hence, as far as probabilities are concerned, the set of positive operators, called the *probability operator measurement* (POM), $\{\Pi_a \equiv M_a^\dagger M_a\}$, is of direct importance.

Evidently, $\sum_a \Pi_a = 1$, and the expression Eq. (1.6), which relates the probabilities of *event* occurrence to the quantum states, is known as *Born's rule*.

More generally, one can do the reverse, in an axiomatic way: Starting by observing the operators $\{\Pi_a = M_a^\dagger M_a\}$ are positive, and demanding $\sum_a \Pi_a = 1$, the expressions of $\text{tr}\{\Pi_a \rho\}$ indeed form a legitimate probability distribution. While it is obvious that any measurement settings can thus be described by a POM, the converse is true as well: Given a POM, it can always be realized, though the actual implementation can be non-trivial. This can be proved as the *Naimark's theorem* [Hay06, Per95]. An example is the Bell measurement for a qubit pair, which requires enlargement of the Hilbert space for additional degrees of freedom [KW98].

IC POM

From the general expression of the statistical operator above, it has the property $\text{tr}\{\rho\} = 1$, as well as being a positive operator, i.e. its expectation value, $\langle |\rho\rangle$, for any $|\rangle$, is always not smaller than zero. These two properties imply that to fully characterize a state, we only need to determine $d - 1$ numbers (recall that the entries of an arbitrary matrix of the same dimension will have $2d$ numbers to be determined, since each entry is generally complex). Physically speaking then, we need to perform measurements to acquire at least d independent *outcomes* to obtain enough information about the state².

Set of measurement operators which provides enough information to characterize an unknown state is called an *informationally complete* (IC) POM. For *minimal* IC POM, exactly d outcomes are measured. Generally, due to the statistical nature of quantum measurement outcomes, measurements on many identical copies of the state are needed in order to obtain a precise and reliable state identification.

1.2.2 Quantum state estimation

The inference and reconstruction of a quantum state from the measurement results is known as *quantum state tomography*. A popular method used is called the *maximum*

²We need d (instead of $d - 1$) independent outcomes because the total number of measured copies are usually not known *a priori*.

likelihood estimation method [Fis22, Hel76].

Maximum likelihood (ML) estimation

Suppose we performed an experiment on a prepared “true” state ρ_{true} , and obtained the frequencies $\{f_j\}$ for the POM $\{\Pi_j\}$. That is, for the outcome labeled j , N_j occurrences were registered out of the total N copies measured, such that $f_j = N_j/N$, and $N = \sum_j N_j$, assuming no losses. By denoting $p_j = \text{tr}\{\Pi_j\rho\}$ as the probability of getting the outcome j for the state ρ , the *likelihood* \mathcal{L} for given ρ to produce the observed data event is then

$$\mathcal{L}(\{N_j\}|\rho) = \prod_j p_j^{N_j}. \quad (1.7)$$

Given no prior knowledge about the system, one estimates the state which maximizes the likelihood, ρ_{ML} , as the true state ρ_{true} . For an IC POM, this *maximum-likelihood* (ML) *estimator* is unique. Ideally, ρ_{ML} should coincide with ρ_{true} , and satisfy $\text{tr}\{\rho_{\text{ML}}\Pi_j\} = p_j = f_j$. Realistically however, there are unavoidable fluctuations in the outcomes due to statistical nature of quantum phenomena, and possibly imperfections in real experimental set-up. It is then almost certain that ρ_{ML} will not coincide with ρ_{true} . Of course, if there is no imperfection in the set-up, when the measurements are performed over a reasonably large number of copies of the system, ρ_{ML} will be close to ρ_{true} , and $\rho_{\text{ML}} \rightarrow \rho_{\text{true}}$ when $N \rightarrow \infty$. That is, ML estimators are *consistent* estimators. Efficient computer algorithms to perform maximum-likelihood quantum state estimation are readily available, as can be obtained from references [PR04, ŘHKL07].

Maximum-likelihood-maximum-entropy (MLME) estimation

If the measurement does not form an IC POM, one could then have many estimators which are consistent with the experimental data with equally high likelihood. To still have a unique identification of the state, additional constraints need to be enforced. One such method is known as the *maximum-likelihood-maximum-entropy* (MLME) scheme, in which after the maximum-likelihood estimation stage, one chooses the estimator that maximizes the von Neumann entropy $S(\rho) = -\text{tr}\{\rho \log_2 \rho\}$ [TZE⁺11,

TSE⁺12]. For a given set of frequencies $\{f_j\}$, this MLME estimator ρ_{MLME} is unique. As the entropy is a measure of uncertainty in a physical system [NC10], the MLME estimator corresponds to the least-bias and most conservative guess for true state consistent with the measurement data.

Fidelity

To measure how “close” the estimator is to the target ρ_{true} , the *fidelity*, F , which generalizes the overlap between two kets, is used [Joz94, NC10]. For any ρ and ρ_0 , the fidelity is given by

$$\begin{aligned} F &= \text{tr} \left\{ \sqrt{\sqrt{\rho} \rho_0 \sqrt{\rho}} \right\} \\ &= \text{tr} \{ |\sqrt{\rho} \sqrt{\rho_0}| \}. \end{aligned} \tag{1.8}$$

Obviously, $F = 1$ when the two states are identical, and $F = 0$ when they correspond to blends of orthogonal states, i.e. $\rho = \sum_j |\phi_j\rangle g_j \langle \phi_j|$, $\rho_0 = \sum_j |\psi_j\rangle f_j \langle \psi_j|$, where $\langle \psi_j | \phi_k \rangle = 0 \forall \{j, k\}$. When both states are pure, F reduces to the absolute value of their overlap, $F = |\langle \psi | \phi \rangle|$.

1.3 Witnesses and entanglement quantification

Entanglement is one active topic of current research, where the quantum correlation between subsystems is at the heart of many interesting fields, like quantum key distribution [Eke91], quantum teleportation [BPM⁺97], and demonstration of various concepts of quantum mechanics [AGR81, CS78]. While it is not our aim here to study various applications and usefulness of quantum entanglement, conscientiously knowing its importance in the above fields, we are concerned with how to efficiently verify whether a state is entangled or separable. For this purpose, we review briefly the geometry of the state space first.

Geometry of quantum states

The set of all separable states is a *convex set*. That is, mixtures of separable states will remain separable, which is both physically and mathematically obvious. An-

other example is the ML *convex set*, i.e. the set of estimators of maximum likelihood obtained from informationally incomplete POM. Mixtures of such estimators maximize the likelihood, as well.

However, the set of entangled states are not convex. A simple counter-example is an equal mixture of $|\Phi^+\rangle = \frac{1}{\sqrt{2}}(|HV\rangle - |VH\rangle)$ with $|\Phi^-\rangle$, which results in $\rho = |\text{HV}\rangle\frac{1}{2}\langle\text{HV}| + |\text{VH}\rangle\frac{1}{2}\langle\text{VH}|$, which is clearly a separable state.

1.3.1 Witness operator

This special closure or convex property of the separable states invites another way of describing entanglement: There must exist [HHH96, Ter00] a Hermitian operator W , called the *entanglement witness* or *witness operator*, such that if the state ρ_0 is entangled,

$$\begin{cases} \text{tr}\{W\rho\} \leq \mu \text{ for all separable states,} \\ \text{tr}\{W\rho\} > \mu \text{ for some entangled states, including } \rho_0. \end{cases} \quad (1.9)$$

μ is called the *threshold* of the witness operator, and when the second inequality above is satisfied, one says that this witness operator *detects* the state ρ . As a concrete example, for a bipartite qubit system, $W = |\Phi^+\rangle\langle\Phi^+|$ is a witness with threshold $\mu = 1/2$.

One particular important kind of witness operator is an *optimal witness* W_{Opt} : No other witnesses can detect *all* the entangled states detected by W_{Opt} , *plus* some other states [LKCH00]. Geometrically, a witness does nothing but defines a hyperplane in the state space, which separates a partial set of entangled states from all other states. Then, an optimal witness defines a hyperplane in the state space which touches the convex set of separable states, see Fig. 1.1 for simple illustration³.

1.3.2 Quantification of entanglement

The singlet Bell ket, $|\Phi^-\rangle$, for example, shows maximum correlation between the two subsystems, independent of the basis of observation. On the other hand, separable

³The figure shown is for demonstration only: The actual convex state space is not elliptical in its boundary as drawn, but generally complex and abstract.

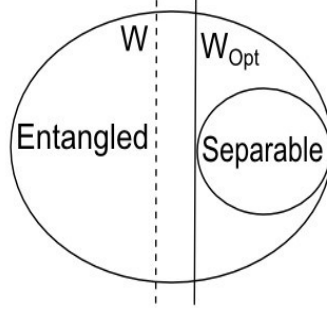


Figure 1.1: Geometry of states and entanglement witnesses.

states preserve individual knowledge about the subsystems, and measurements shall review no such quantum correlation among them. Naturally then, one expects some quantitative measures of entanglement, which vary smoothly from separable to maximally entangled states. Indeed, there are a plethora of such measures, stemmed from various (geometrical, algebraic, operational) considerations [BŻ06].

For our work, we choose to use the *concurrence* C , and its square, the *tangle* T , which for bipartite qubit, has the advantage of having available analytical expressions, as our basic measures of entanglement [Woo98, CKW00]. The analytical expression for concurrence is

$$C[\rho] = \max\{0, \lambda_1 - \lambda_2 - \lambda_3 - \lambda_4\}, \quad (1.10)$$

where λ_j 's are the eigenvalues, in decreasing order, of the Hermitian matrix $R \equiv \sqrt{\sqrt{\rho}\tilde{\rho}\sqrt{\rho}}$. Here, $\tilde{\rho} = \Sigma\rho^T\Sigma$, where ρ and $\Sigma = Y \otimes Y$, Y being the y -Pauli operator, all are expressed in the *standard basis* $\{|VV\rangle, |VH\rangle, |HV\rangle, |HH\rangle\}$, i.e.

$$\begin{aligned} \Sigma = Y \otimes Y &= \begin{array}{c} \langle V| \quad \langle H| \\ |V\rangle \begin{pmatrix} 0 & -i \\ i & 0 \end{pmatrix} \\ |H\rangle \end{array} \otimes \begin{array}{c} \langle V| \quad \langle H| \\ |V\rangle \begin{pmatrix} 0 & -i \\ i & 0 \end{pmatrix} \\ |H\rangle \end{array} \\ &= \begin{array}{c} \langle VV| \quad \langle VH| \quad \langle HV| \quad \langle HH| \\ |VV\rangle \begin{pmatrix} 0 & 0 & 0 & -1 \\ |VH\rangle \begin{pmatrix} 0 & 0 & 1 & 0 \\ |HV\rangle \begin{pmatrix} 0 & 1 & 0 & 0 \\ |HH\rangle \begin{pmatrix} -1 & 0 & 0 & 0 \end{pmatrix} \end{pmatrix} \end{pmatrix} \end{array}. \quad (1.11) \end{aligned}$$

For all separable states, their concurrences are zero, and for maximally entangled states, $C = 1$.

Entanglement of formation

The reason why the concurrence is a measure of entanglement is not so obvious from its expression alone⁴. To make the connection, we need the concept of the *entanglement of formation*, which is intended to quantify the resources needed to create a given entangled state [BDSW96, Woo98].

Consider a bipartite qubit system described by ρ . If one of the subsystems, called A, is measured with Π_j , the probability of this outcome is then

$$\begin{aligned} p_j &= \text{tr}\{\rho(\Pi_j^A \otimes \mathbb{1}^B)\} \\ &= \text{tr}_A \text{tr}_B\{\rho(\Pi_j^A \otimes \mathbb{1}^B)\} = \text{tr}_A\{\Pi_j^A \text{tr}_B\{\rho\}\}, \end{aligned} \quad (1.12)$$

where the superscripts A, B label the two subsystems, and tr_A is partial trace w.r.t subsystem A, for instance. Without making reference to subsystem B, the statistical operator describing A is thus $\rho_A \equiv \text{tr}_B\{\rho\}$. For pure states, if $\rho = |\psi\rangle\langle\psi|$ is entangled, then ρ_A must be a mixed state, since A admits no description by purely a ket. The higher the mixedness of ρ_A , the more entangled ρ is. Another natural measure of the mixedness, besides the purity, is the von Neumann entropy, $S(\rho)$. $S(\rho) = 0$ if and only if ρ is pure, and $S(\rho) = 1$ for a maximally entangled state. Since any bipartite ket $|\psi\rangle$ admits a Schmidt decomposition, i.e. it can always be written as $|\psi\rangle = \sum_j \sqrt{p_j} |j\rangle_A |\bar{j}\rangle_B$ with $\sum_j p_j = 1$ for some kets $|j\rangle_A$ and $|\bar{j}\rangle_B$, where the sets of kets $|j\rangle_A$ and $|\bar{j}\rangle_B$ form orthogonal bases in their individual Hilbert spaces for subsystems A and B, we can then define the amount of entanglement E for pure states as the entropy of either of the two subsystems A and B:

$$0 \leq E(|\psi\rangle\langle\psi|) = -\text{tr}(\rho_A \log_2 \rho_A) = -\text{tr}(\rho_B \log_2 \rho_B) = -\sum_j p_j \log_2 p_j \leq 1. \quad (1.13)$$

For mixed states, the entanglement of formation E_F is the generalization of E above.

⁴For the author, that is.

First, write $\rho = \sum_i |i\rangle g_i \langle i|$, and consider all its possible blends. E_F is then defined as the (weighted) average entanglement of the pure states of the decomposition, minimized over all the as-if realities:

$$E_F(\rho) = \min \sum_i g_i E(|i\rangle \langle i|). \quad (1.14)$$

Note that $E_F = 0$ if and only if ρ admits at least one possible realization by blends of factorizable states, i.e. ρ is separable. Also, if ρ is pure, E_F reduces to E above. E_F can then be considered as the amount of entanglement needed to create ρ , or the least expected entanglement of any ensemble of pure states realizing ρ .

The minimization problem of E_F is extremely difficult to solve, but fortunately, for a bipartite qubit system, an explicit formula can be given. It is given by [Woo98]

$$E_F(\rho) = - \left(\frac{1 + \sqrt{1 - C^2}}{2} \right) \log_2 \left(\frac{1 + \sqrt{1 - C^2}}{2} \right) - \left(\frac{1 - \sqrt{1 - C^2}}{2} \right) \log_2 \left(\frac{1 - \sqrt{1 - C^2}}{2} \right), \quad (1.15)$$

where C is the concurrence given in Eq. (1.10). Since $E_F(\rho)$ is a monotonic function of C , the concurrence is therefore a justified entanglement measure in its own right.

Chapter 2

Background Concepts II

This chapter introduces further concepts that are directly related to the project and the experiment performed. They include the principles of the entanglement-detection scheme that our experiment shall perform, topics on realization of two-photon polarizations as quantum systems, and the implementation of witness-family measurements.

2.1 Principles of entanglement detection

Entanglement verification in this experiment is in essence comprised of three major principles.

- Firstly, we try to detect entanglement in a straightforward manner through a set of independent *witness-family measurements*. This is done by checking an inequality criterion that is based on the very definition of entanglement witnesses.
- The set of witness bases above are chosen to form an IC POM. Then, secondly, when the state is not detectable individually by such inequalities, we perform quantum state tomography to obtain the ML estimator. We can then evaluate the concurrence or the tangle of the estimator to determine its separability.
- Thirdly, we introduce an “add-on package” to the above two principles. In essence, before the IC POM is realized, we make use of partial information obtained from each witness-family measurement to assist the detection scheme.

2.1.1 Detection of entanglement by witness basis

Witness basis for bipartite qubit system

For a two-qubit system, it can be shown that one can construct a class of optimal witness operators, $W_{\text{Opt}}(\alpha)$, such that their eigenkets are *two product kets* and *two Bell kets*. For details, please see Appendix A.

In summary, in terms of polarization qubits, such a witness basis is given by

$\{|\text{VV}\rangle\langle\text{VV}|, |\text{HH}\rangle\langle\text{HH}|, |\Phi^+\rangle\langle\Phi^+|, |\Phi^-\rangle\langle\Phi^-|\}$. Their associated eigenvalues are $(p - 1)/2, (-1 - p)/2, -q/2, q/2$ respectively, where p and q are related by $p = \sqrt{1 - q^2}$, and $0 < \alpha = \frac{1}{2} \arcsin(q) \leq \frac{\pi}{4}$. Its witness threshold is $\mu = 0$.

The ability to obtain witness operators with such simple eigenbasis shall proved to be useful and crucial for our project. Since eigenvalues are just numbers associated with the eigenvectors, measurement in the eigenbasis is effectively providing measurement results for a class of operators. That is, we are in fact measuring a whole one-parameter *family* of witnesses in one-go. Hence, we shall describe measurements performed on eigenbasis of such optimal witness as “witness-basis measurements”, or equivalently, “witness-family measurements”. In addition, a simple criterion to detect entanglement can be obtained by considering such witness-family measurements.

Entanglement criterion

Recall that for a given state ρ , it is entangled when the measurement results confirms $\text{tr}\{W\rho\} > \mu$. For the optimal witnesses above, we then have the *violation* of the inequality $\text{tr}\{\rho W_{\text{opt}}(\alpha)\} \leq 0$ as the detection criterion for $W_{\text{opt}}(\alpha)$.

Now, since the measurement is the same for all witness parameter α , we can apply a stricter criterion, by which detection of entanglement is indicated by the violation of

$$\min_{\alpha} \left\{ \text{tr}\{-\rho W_{\text{opt}}(\alpha)\} \right\} \geq 0. \quad (2.1)$$

Denoting the expectation values $p_1 = \text{tr}\{\rho|\text{VV}\rangle\langle\text{VV}|\}$, $p_2 = \text{tr}\{\rho|\text{HH}\rangle\langle\text{HH}|\}$, $p_3 = \text{tr}\{\rho|\Phi^+\rangle\langle\Phi^+|\}$ and $p_4 = \text{tr}\{\rho|\Phi^-\rangle\langle\Phi^-|\}$, we have

$$\begin{aligned}
& \min_{\alpha} \left\{ \text{tr} \{ -\rho W_{\text{Opt}}(\alpha) \} \right\} \\
&= \min_{\alpha} \left\{ p_1 \cos^2(\alpha) + p_2 \sin^2(\alpha) + (p_3 - p_4) \sin(\alpha) \cos(\alpha) \right\} \\
&= \min_{\alpha} \left\{ \frac{p_1 + p_2}{2} + \underbrace{\left(\frac{p_3 - p_4}{2} \sin(2\alpha) + \left(\frac{p_1 - p_2}{2} \right) \cos(2\alpha) \right)}_{\frac{1}{2} \sqrt{(p_1 - p_2)^2 + (p_3 - p_4)^2} \sin \left(2\alpha + \tan^{-1} \left(\frac{p_1 - p_2}{p_3 - p_4} \right) \right)} \right\} \\
&= \frac{p_1 + p_2}{2} - \frac{1}{2} \sqrt{(p_1 - p_2)^2 + (p_3 - p_4)^2}. \tag{2.2}
\end{aligned}$$

Thus, the witness criterion now reduces to the simple inequality

$$\mathcal{S}(p_1, p_2, p_3, p_4) \equiv 4p_1 p_2 - (p_3 - p_4)^2 \geq 0. \tag{2.3}$$

In our experiment, we measure the frequencies f_j for the four eigenkets, and then evaluate $\mathcal{S}(f_1, f_2, f_3, f_4)$ to check for the witness criterion. This is justified for measurements performed over a large number of copies of the quantum state.

2.1.2 Witness bases as IC POM

For a fixed basis, Eq. (2.3) is a sufficient but not necessary criterion for entanglement detection. That is, an entangled quantum state need not violate it. If this is the case, we then need to perform another measurement, using a different optimal witness basis, and check the inequality again. This can be achieved by performing local unitary transformations to the initial witness basis¹. If we were to rely on each measurement separately, we would have to measure infinitely many witnesses to obtain conclusive results. This problem can however be overcome, if we measure witnesses that form IC POM. As mentioned in Sec. 1.2.1, here, at least 16 independent measurement outcomes are needed to form an IC POM.

In this respect, the elegance of measuring witness bases shines once more: By one such measurement, one gets *three* independent outcomes. As one can verify directly, for the witness basis given above, the set of corresponding observables are

¹Or equivalently, we are changing the quantum states by local unitary transformations, and still measure in the same old witness basis. Note that *local* unitary transformations do not change the amount of entanglement.

$\{Z\mathbb{1} + \mathbb{1}Z, ZZ, XX + YY\}$. Here, X, Y , and Z are the standard Pauli operators

$$\begin{aligned} X &= |v\rangle\langle H| + |H\rangle\langle v|, \\ Y &= |H\rangle i\langle v| - |v\rangle i\langle H|, \\ Z &= |v\rangle\langle v| - |H\rangle\langle H|, \end{aligned} \tag{2.4}$$

and product such as $Z\mathbb{1}$, for instance, means that Z is applied on the first qubit and the identity $\mathbb{1}$ on the second qubit. To obtain the rest 12 observables, we perform unitary operations by applying U_1 and U_2 to the first and second qubit respectively. A summary of the unitary operators applied, and the observables thus obtained, is provided in Table 2.1, taken from [ZTE10].

Witness	U_1	U_2	Observables
1	$\mathbb{1}$	$\mathbb{1}$	$Z\mathbb{1} + \mathbb{1}Z, ZZ, XX + YY$
2	$\mathbb{1}$	X	$Z\mathbb{1} - \mathbb{1}Z, ZZ, XX - YY$
3	C^\dagger	C	$X\mathbb{1} + \mathbb{1}Z, XY, YZ + ZX$
4	C^\dagger	XC	$X\mathbb{1} - \mathbb{1}Z, XY, YZ - ZX$
5	C	C^\dagger	$Y\mathbb{1} + \mathbb{1}X, YX, ZY + XZ$
6	C	XC^\dagger	$Y\mathbb{1} - \mathbb{1}X, YX, ZY - XZ$

Table 2.1: The six witnesses that collectively form an IC POM, and the unitary operators relating them.

Here, C is the *Clifford operator* that permutes the Pauli operators cyclically, i.e. $CX = YC, CY = ZC, CZ = XC$. More explicitly, we have

$$C = \frac{1}{2}(\mathbb{1} - iX - iY - iZ) = e^{-i\frac{\pi}{3}\mathbf{J} \cdot \boldsymbol{\sigma}}, \tag{2.5}$$

where $\mathbf{J} = \frac{1}{\sqrt{3}}(\mathbf{e}_x + \mathbf{e}_y + \mathbf{e}_z)$ is the unit vector along the 1-1-1 axis, and $\boldsymbol{\sigma}$ are the Pauli operators, in compact vectorial notation.

As a summary: Measurements on six witnesses are needed at most to detect entanglement, should each of the entanglement-detection criteria Eq. (2.3) fail. Since these six witnesses form an IC POM, state tomography can be performed to obtain the ML estimator. One can then evaluate its tangle to check its separability.

2.1.3 Adaptive schemes

Suppose we start with witness 1 in Table 2.1, and inequality Eq. (2.3) is not violated. The question is, which witness should we choose for the next measurement? Of course, the simplest way is to pick the next one at random; let's call this strategy the Scheme A. On the other hand, aiming at reducing the average number of witness-family measurements needed, one can expect that the Scheme A is rather ineffective. Indeed, by making use of the information about the quantum state obtained from previous measurement(s), there is an economic way of choosing the next basis, which allows us to speed up the detection of entanglement [Teo13]. This is done by choosing the witness with highest chance of violating the inequality as our next measurement setting, which we summarize as the Scheme B below.

Adaptive scheme with no separability test (Scheme B)

1. First, randomly start with a witness from Table 2.1, and obtain the experimental frequencies f_j for the eigenkets. If Eq. (2.3) is violated, then entanglement is detected.
2. If Eq. (2.3) is not violated, perform quantum state tomography with the experimental frequencies to obtain the MLME estimator.
3. Evaluate the probabilities p_j for the other five witnesses using $\rho = \rho_{\text{MLME}}$.
4. Choose the witness which has the smallest value of $\mathcal{S}(p_1, p_2, p_3, p_4)$. This corresponds to the highest chance of violating the inequality, consistent with the information available.

If the detection criterion Eq. (2.3) is not violated for the second witness, repeat the scheme, but with the frequencies collected from all previous witnesses are used for construction of the MLME estimator. Repeat this scheme until Eq. (2.3) is violated for one witness, or else, after six witnesses, obtain the ML estimator and evaluate its tangle directly.

Adaptive scheme with separability test (Scheme C)

On top of the Scheme B, we can introduce an additional step for further improvement. This is summarized as the Scheme C below.

- Compare the likelihood, Eq. (1.7), using ρ_{MLME} , with the maximum likelihood attainable for all separable states.
- If the former is larger than the latter, this means the ML convex set contains no separable states. The state is then determined to be entangled, since any subsequent witness measurements correspond to reducing the dimension and size of the ML convex set, and ultimately to a point estimator (the ML estimator) for IC POM. This is true when the copies of quantum states measured are large.

2.2 Photon polarization as qubit

Success in realizing bipartite photonic quantum systems relies fundamentally on a nonlinear optical phenomena, called the *Spontaneous Parametric Down-Conversion* (SPDC).

2.2.1 Source of biphoton: SPDC

A non-magnetic dielectric crystal, with no inversion symmetry, such as beta barium borate (BBO), has a property of nonlinear susceptibility [DGN99]. That is, when the electric field \mathbf{E} that passes through the material has high intensity, e.g. electromagnetic (EM) waves of a strong laser beam, the material exhibits nonlinear responses, such that the electric displacement vector \mathbf{D} is not linearly proportional to the \mathbf{E} . That is, one has [MW95]

$$\mathbf{D} = \epsilon_0 \mathbf{E} + \mathbf{P}, \quad (2.6)$$

where $\epsilon_0 = 8.854 \times 10^{-12}$ F/m is the vacuum permittivity and \mathbf{P} is the polarization vector, expressible as power series in \mathbf{E} :

$$P_i = \chi_{ij}^{(1)} E_j + \chi_{ijk}^{(2)} E_j E_k + \chi_{ijkl}^{(3)} E_j E_k E_l + \dots \quad (2.7)$$

$\chi^{(n)}$ is the susceptibility tensor of rank $n+1$, and is associated with *nonlinear effects* of n -th order. One particular second-order nonlinear phenomena is the SPDC—spontaneous generation of two photons from a single photon of higher energy. The full and rigorous description of SPDC is a quantum electrodynamics exercise [MW95, HM84, Blo96], which is rather non-trivial and not at the focus of our project. Here, we shall be content with the following phenomenological description of SPDC.

In the crystal, a mother photon, called the *pump*, of frequency ω_p and wave vector \mathbf{k}_p , spontaneously decay into two daughter (conventionally called *signal* and *idler*) photons $(\omega_s, \mathbf{k}_s; \omega_i, \mathbf{k}_i)$, see Fig. 2.1 for illustration. Conservation of energy and momentum read

$$\hbar\omega_p = \hbar\omega_s + \hbar\omega_i, \quad (2.8)$$

$$\hbar\mathbf{k}_p = \hbar\mathbf{k}_s + \hbar\mathbf{k}_i. \quad (2.9)$$

Consider the case of degenerate down conversion, i.e. $\omega_s = \omega_i$. Then, using the relationship $k \equiv |\mathbf{k}| = n\omega/c$ between the wave number and the frequency, where n is the refractive index for frequency ω and c is speed of light in vacuum, we get

$$\omega_p = 2\omega_s = 2\omega_i, \quad (2.10)$$

$$k_p^2 = \left(\frac{n_p\omega_p}{c}\right)^2 = \left(\frac{n_s\omega_p}{2c}\right)^2 + \left(\frac{n_i\omega_p}{2c}\right)^2 + 2\left(\frac{n_s n_i \omega_p^2}{4c^2}\right) \cos \vartheta, \quad (2.11)$$

where ϑ is the angle between \mathbf{k}_s and \mathbf{k}_i . For $\vartheta \neq 0$, we have *non-collinear* SPDC. Since $n_s = n_i$, Eq. (2.11) reads

$$n_p^2 = n_s^2 \cos^2 \frac{\vartheta}{2}, \quad (2.12)$$

which shows that n_s needs to be at least not smaller than n_p . This condition can be satisfied in crystals with *birefringence* properties.

Birefringence

Excellent coverage of the subject of birefringence or double refraction is available at the classic books of Born&Wolf [BW99], and Landau [Lan98]. In essence, an EM

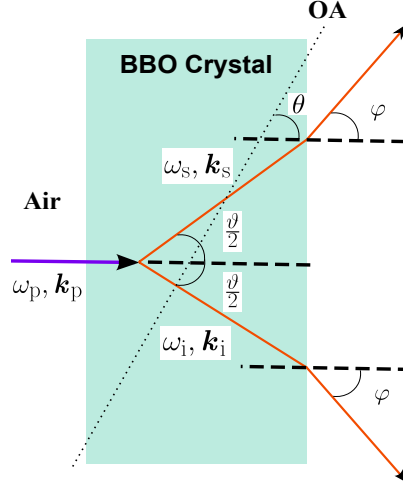


Figure 2.1: Non-collinear degenerate SPDC: A two-dimensional illustration. Inside the BBO crystal, the pump photon is spontaneously down-converted into signal and idler photons of degenerate wavelength. The crystal’s optic axis and the pump’s polarization are both in the plane of the page, making the pump an extraordinary ray. The signal and idler have polarizations perpendicular to the page, i.e. they are ordinary rays. This is known as Type-I phase matching, or ‘e \rightarrow o+o’ configuration. In reality, there is a rotational symmetry around the axis of \mathbf{k}_p , so SPDC is observed as rings in three-dimensional space, where φ is called the *cone-opening angle*.

wave traveling from vacuum into the birefringent crystal will generally be refracted and subsequently propagate in *two* different directions, with orthogonal linear polarizations. One of the refracted waves, called the *ordinary ray*, always propagates at a fixed speed, while the second refracted wave, called the *extraordinary ray*, travels at the speed that depends on the *phase-matching angle* θ between the incident wave vector and the *optic axis* (OA) of the crystal². Equivalently, the two refracted waves experience different refractive indices, labeled as n_o and $n_e(\theta)$. Crystals with $n_o \geq n_e(\theta)$ are known as *negative* crystals.

Phase matching

Equation (2.12) can now be satisfied, by using a negative crystal, such as BBO crystal. This is done by specifically choosing the orientation of its optic axis such that the pump travels as extraordinary ray with $n_p = n_e(\omega_p, \theta)$, and the down-converted light are produced as ordinary rays with $n_s = n_o(2\omega_p)$. Due to dispersive property of material, $n_o(2\omega)$ is usually only slightly larger than $n_e(\omega)$, hence restricting the

²We are considering uniaxial crystals only, and thus there is only one such axis.

angle ϑ in Eq. (2.12) at small values. The above conditions used to produce SPDC are known as Type-I *phase-matching conditions*. Finer discussions on birefringence and analytic calculation for phase-matching conditions are included in Appendix B.

NIST Phasematch

Another efficient approach to obtain phase-matching conditions is by using available free software, namely the *NIST Phasematch* programme, developed by National Institute of Standards and Technology, U.S. Department of Commerce. By keying in the values of the relevant parameters, such as the phase-matching angle θ etc., the software will generate intensity plot of the down-converted light, as function of wavelength and the *cone-opening angle* φ in Fig. 2.1 above. A snapshot of the programme is provided in Fig. 2.2.

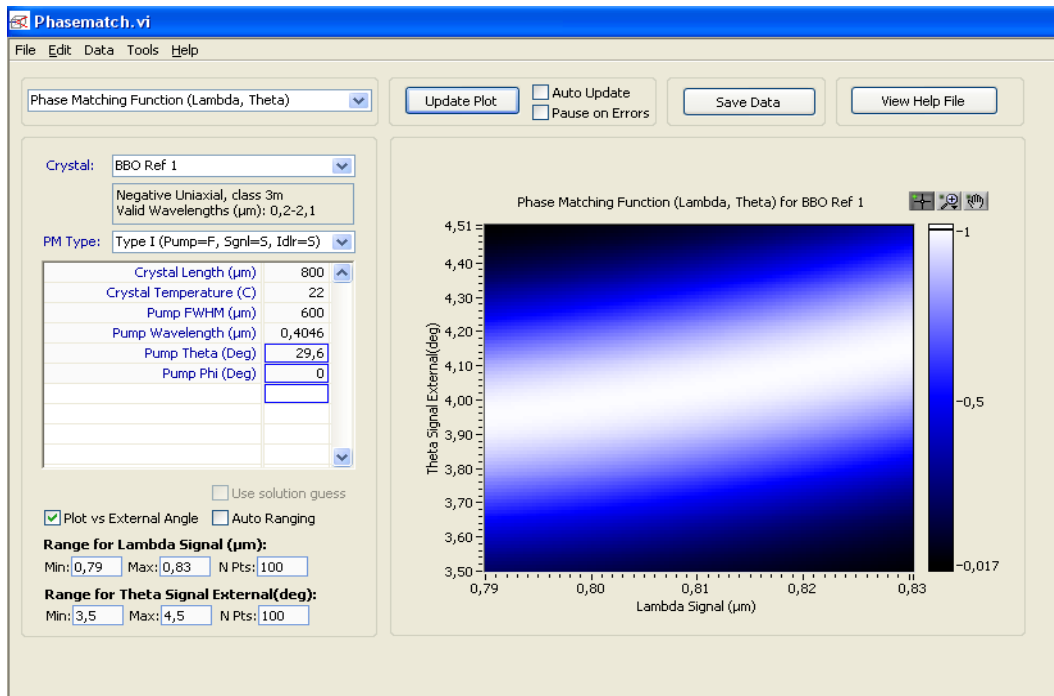


Figure 2.2: *NIST Phasematch* software: By choosing the appropriate subjects or functions from the database, as shown in the picture are Type-I phase matching using BBO crystal, and inserting relevant values such as the crystal's thickness ($800 \mu\text{m}$), the pump's wavelength (404.6 nm), its full width at half maximum (0.6 mm) and the phase-matching angle θ (29.6°), the intensity spectra of the down-converted light as a function of wavelength and cone-opening angle φ can be obtained. As can be seen from the image, with the optic axis cut at 29.6° , most of the down-converted light emerged at an angle $\varphi \approx 4^\circ$.

2.2.2 Polarization manipulations using optical devices

In this project, polarization of the photon is our main quantum degree of freedom, and its manipulations is done by using wave plates and beam splitters. For definiteness, the polarizations are defined according to the optical table's reference frame. That is, for light traveling parallel to the table surface, horizontal refers to a direction contained in the plane, while vertical refers to a direction perpendicularly up to the table surface.

Wave plates

Wave plates (WPs), or *retarders*, change the polarization. The principle of operation of a retarder is rather simple: It divides an incident, polarized beam into two linear components, changes their relative phase, then recombines them. Because of the phase shift, the recombined beam thus has a new polarization, in general. This change of relative phase can be accomplished by making the two components travel at different speeds, i.e. experiencing different refractive indices. Evidently, a birefringent material (usually quartz) is a good candidate for this purpose. The component that travels faster defines the *fast axis* (for quartz, this is also the optic axis), while the *slow axis* is defined by the corresponding slower component. These two axes are orthogonal, and are made to form a plane perpendicular to the incident light. Making reference to the lab's coordinate, we calibrate the wave plates by the angle θ between their fast axes and the vertical direction. It is 0° when the fast axis is vertical, and 90° when it is horizontal, rotate in the anti-clockwise sense.

A *half-wave plate* (HWP) is a retarder whose thickness is cut such that the retardance between the two beams is exactly π . The associated unitary operator describing a HWP orientated at angle θ is then given by

$$\begin{aligned} U_{\text{HWP}}(\theta) &= \begin{pmatrix} |V\rangle & |H\rangle \end{pmatrix} \begin{pmatrix} \cos(2\theta) & \sin(2\theta) \\ \sin(2\theta) & -\cos(2\theta) \end{pmatrix} \begin{pmatrix} \langle V| \\ \langle H| \end{pmatrix} \\ &\cong \begin{pmatrix} \cos(2\theta) & \sin(2\theta) \\ \sin(2\theta) & -\cos(2\theta) \end{pmatrix}, \end{aligned} \quad (2.13)$$

apart from irrelevant global phase factor.

A *quarter-wave plate* (QWP) is another standard retarder, where the phase difference between the two beams is $\pi/2$. Expressed in the standard basis, a QWP is represented by the matrix

$$U_{\text{QWP}}(\theta) \hat{=} \frac{1}{\sqrt{2}} \begin{pmatrix} 1 - i \cos(2\theta) & -i \sin(2\theta) \\ -i \sin(2\theta) & 1 + i \cos(2\theta) \end{pmatrix}. \quad (2.14)$$

As an interesting and important remark, an *arbitrary* polarization transformation can be achieved by sending the photon through a QWP, then through a HWP, and finally through another QWP [EKW01].

Beam splitters

A *beam splitter* or partially-reflecting mirror, is a piece of material (e.g. fused silica) that transmits and reflects light, with a specific ratio $T : R$, where $T + R = 1$, with negligible losses. A beam splitter which reflects and transmits light independent of their polarizations is known as a *non-polarizing beam splitter* (BS). Another kind of beam splitter is known as *polarizing beam splitter* (PBS). It reflects photons with vertical polarization, and transmits photon with horizontal polarization.

2.3 Realization of a witness-basis measurement

We now discuss the realization of a witness-basis measurement, using our optical devices.

2.3.1 Hong-Ou-Mandel interferometer as witness basis

Consider a $R : T$ BS, with losses negligible. At the scale of single photon, this means the chances it will be reflected or transmitted is in ratio the $R : T$. As upon measurement, a photon can only be either on the left side or the right side of the BS, we can describe this *path* (or position) degree of freedom effectively as a qubit system³. That is, we have the orthogonal kets $\{|a\rangle_{\text{L}}, |a\rangle_{\text{R}}\}$ describing a *left qubit* and a *right qubit* respectively, where “ a ” specifies the various properties (including

³As a side note, one can use the propagation of light (*going* left or right) to define the path qubit, but of course the physics remains the same.

polarization) carried by the photon. Assuming a symmetric beam splitter (i.e. its two sides are of no difference) which does not distinguish the properties “ a ”, the quantum mechanical description of the BS is then

$$U_{\text{BS}} = \begin{matrix} & \langle |_{\text{L}} & \langle |_{\text{R}} \\ \begin{matrix} | \rangle_{\text{L}} \\ | \rangle_{\text{R}} \end{matrix} & \begin{pmatrix} i\sqrt{R} & \sqrt{T} \\ \sqrt{T} & i\sqrt{R} \end{pmatrix} \end{matrix}. \quad (2.15)$$

More interestingly, instead of single photon, one can incident another photon from the other side of the BS, such that the reflected and transmitted light propagate exactly the same path as the transmitted and reflected light, respectively, of the previous incident light. Then, we have essentially a two-qubit system. Before the two photons meet, on one side of the BS, there is a left qubit $|a\rangle_{\text{L}}$, and on the other side, a right qubit $|b\rangle_{\text{R}}$. When they strike on, the BS acts as a *unitary scatterer*:

$$|a\rangle_{\text{L}} \longrightarrow \sqrt{T}|a\rangle_{\text{R}} + i\sqrt{R}|a\rangle_{\text{L}}, \quad |b\rangle_{\text{R}} \longrightarrow \sqrt{T}|b\rangle_{\text{L}} + i\sqrt{R}|b\rangle_{\text{R}}. \quad (2.16)$$

Using Fock states $|n, m\rangle$ to represent n photons in the “mode” staying at left side of the BS, and m photons staying at the right side, we take note of the following three cases: (notation: $|a\rangle_{\text{L}} \otimes |b\rangle_{\text{R}} \equiv |ab\rangle$)

- ‘Separable’ input: $|ab\rangle$, a and b are equal,
 Output: $-R|ab\rangle + T|ba\rangle + i\sqrt{RT}(|a\rangle_{\text{L}}|b\rangle_{\text{L}} + |a\rangle_{\text{R}}|b\rangle_{\text{R}})$
 $\equiv \frac{(T-R)}{\sqrt{T^2+R^2}}|ab\rangle + i\frac{\sqrt{RT}}{\sqrt{T^2+R^2}}(|0, 2\rangle + |2, 0\rangle)$.
 Special case, $R = T = \frac{1}{2}$: \rightarrow *bunching* to one path.
- Indistinguishable entangled ‘bosonic’ input: $\frac{1}{\sqrt{2}}(|ab\rangle + |ba\rangle) \equiv |1, 1\rangle$, a and b have *orthogonal* polarizations,
 Output: $\frac{T-R}{\sqrt{2}}(|ab\rangle + |ba\rangle) + i\sqrt{2RT}(|a\rangle_{\text{L}}|b\rangle_{\text{L}} + |a\rangle_{\text{R}}|b\rangle_{\text{R}})$
 $\equiv (T-R)|1, 1\rangle + i\sqrt{2RT}(|2, 0\rangle + |0, 2\rangle)$.
 Special case, $R = T = \frac{1}{2}$: \rightarrow *bunching* to one path.
- Indistinguishable entangled ‘fermionic’ input: $\frac{1}{\sqrt{2}}(|ab\rangle - |ba\rangle) \equiv |1, 1\rangle$, a and b have *orthogonal* polarizations,
 Output: $-\frac{1}{\sqrt{2}}(|ab\rangle - |ba\rangle) \equiv -|1, 1\rangle \rightarrow$ *splitting* to different paths.

These *interference* effects, though usually referred to the “bosonic” type only, are known as *Hong-Ou-Mandel effect(s)* [HOM87]. By now, the exact correspondence between product states, Bell kets $|\Phi^+\rangle$ and $|\Phi^-\rangle$ with the three cases above should be obvious. Hence, by putting one PBS at each arm after a 50:50 BS, it is obvious that one is able to measure all the four eigenkets of the witness operator, through the following distinctive features; see Fig. 2.3 as well.

Eigenket	Photon counts (LH,LV,RH,RV)
$ \text{HH}\rangle$	(2,0,0,0) or (0,0,2,0)
$ \text{VV}\rangle$	(0,2,0,0) or (0,0,0,2)
$ \Phi^+\rangle$	(1,1,0,0) or (0,0,1,1)
$ \Phi^-\rangle$	(1,0,0,1) or (0,1,1,0)

Table 2.2: Signatures of eigenkets of the witness operators.

A remark: When the two photons are not *indistinguishable*, i.e. by carefully studying their arrival times, frequencies, polarizations, or any other properties, such that one is able to tell, in principle, whether the photons were originally left or right qubits, there will be no interference effects observed. This is Bohr’s *principle of complementarity* [Boh28, Sch60, Eng96]. For such distinguishable situations, in the above cases, the photons are equally likely to bunch, or split.

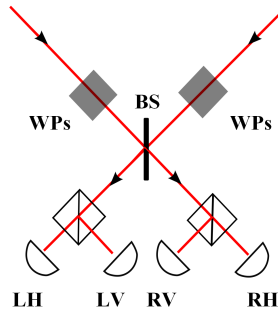


Figure 2.3: Realization of a witness-basis measurement using HOM interferences, with the signatures given in the Table 2.2. As an example, when the detectors at LH and LV ports both register photons simultaneously, this corresponds to a measurement signature for the $|\Phi^+\rangle$ eigenket. The wave plates WPs are used to change the witness basis for subsequent measurements, see Sec. 2.3.2.

2.3.2 Change of witness basis to form POM

The previous discussion focuses on witness 1 in Table 2.1. To measure in the other five bases, WPs, in the order of QWP-HWP-QWP, are installed at both input arms to implement the unitary operators given in Table 2.1. The required angles for the WPs to perform the unitary operations are summarized below:

$$\begin{aligned}
\mathbb{1} &= U_{\text{QWP}}(0)U_{\text{HWP}}(0)U_{\text{QWP}}(0) \hat{=} \begin{pmatrix} 1 & 0 \\ 0 & 1 \end{pmatrix}, \\
X &= U_{\text{QWP}}(0)U_{\text{HWP}}(\frac{\pi}{4})U_{\text{QWP}}(0) \hat{=} \begin{pmatrix} 0 & 1 \\ 1 & 0 \end{pmatrix}, \\
C &= U_{\text{QWP}}(0)U_{\text{HWP}}(\frac{\pi}{4})U_{\text{QWP}}(\frac{-\pi}{4}) \hat{=} \frac{1}{\sqrt{2}} \begin{pmatrix} 1 & -i \\ 1 & i \end{pmatrix}, \\
C^\dagger &= U_{\text{QWP}}(\frac{-\pi}{4})U_{\text{HWP}}(0)U_{\text{QWP}}(0) \hat{=} \frac{1}{\sqrt{2}} \begin{pmatrix} 1 & 1 \\ i & -i \end{pmatrix}, \\
XC &= U_{\text{QWP}}(0)U_{\text{HWP}}(0)U_{\text{QWP}}(\frac{-\pi}{4}) \hat{=} \frac{1}{\sqrt{2}} \begin{pmatrix} 1 & i \\ 1 & -i \end{pmatrix}, \\
XC^\dagger &= U_{\text{QWP}}(\frac{\pi}{4})U_{\text{HWP}}(0)U_{\text{QWP}}(0) \hat{=} \frac{1}{\sqrt{2}} \begin{pmatrix} i & -i \\ 1 & 1 \end{pmatrix}. \tag{2.17}
\end{aligned}$$

In the above equalities, we have ignored any irrelevant global phase. Note that the matrix operation is always from right to left, i.e. the U_{QWP} on the left corresponds to the QWP that is closer to the BS in Fig. 2.3.

Part II

Experiment

Chapter 3

Witness-Family Measurements

Our experiment can be operationally divided into three stages: At first, there is the controllable generation of two-photon polarization states, and at the end, there is the detection of the photons using photon detectors, thereby completing the measurement with the witness basis. In between these two, we have the manipulations of photon polarization, leading to their interference at the beam splitter. In this chapter, we describe, in detail, our effort in carrying out the experiment, according to these three stages.

As a remark, all our experiments are performed on an optical table with tuned damping (Newport, RS 2000), over a surface area of 1200×1800 (mm).

3.1 Generation of two-photon states

To understand the experimental performances of the entanglement-detection scheme, we generate three different classes of states as test sources. They are states of different ranks, namely rank-1 states, rank-2 states, and rank-4 states. Inasmuch the technical aspects in generating these 3 classes of states are all slightly different, they share the same photon sources and most of their experimental set-up. In fact, they are all modified from a standard Bell state generation set-up which uses two-Type-I crystal geometry [KWW⁺99]. Meanwhile, as the generation of rank-4 states is more complicated, its discussion shall be postponed to Sec. 3.4.

3.1.1 Bell states

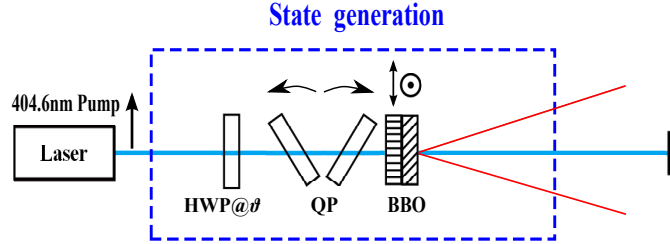


Figure 3.1: Schematic for the generation of the Bell states and rank-1 states. A C-W diode laser pumps two type-I BBO crystals with optic axes on orthogonal planes, and the SPDC occurs in the non-collinear frequency-degenerate regime. When the HWP is set at 22.5° , it changes the vertically polarized pump photons to -45° , and thereby produces the Bell states. To generate the class of rank-1 states given in Eq. (3.2), the HWP is set at ϑ . quartz plates (QP) are used to control the relative phase between the generated states from the two crystals.

The schematic experimental set-up to generate Bell states is shown in Fig. 3.1. Two similar BBO crystals of both $5 \times 5 \times 0.8$ (mm) in length, width and thickness are mounted together on a tunable stage (KM100PM, Thorlabs). The optic axes of the first and second crystals are oriented in the vertical and horizontal planes respectively, both making angles of 29.5° w.r.t. the pump's propagation \mathbf{k}_p , which is incident on the crystals normally. The pump originates from a frequency-stabilized continuous-wave (C-W) diode laser (ONDAX, LM Series, ≈ 40 mW) at a wavelength of 404.6 nm, or frequency $\nu = 7.410 \times 10^{14}$ Hz, with beam size of about 0.8×0.6 (mm), slightly elliptical in shape. The laser is vertically polarized with intensity ratio $> 100 : 1$ over its horizontal component, and is reported to have a *linewidth* of about $\Delta\nu = 160$ MHz. Equivalently, the *coherence length* of the pump laser is about $L_c = 1.87$ m¹. To increase the yield of down-converted photons, we place a lens of focal length 50 mm to focus the pump laser at the crystals.

By using a HWP at 22.5° , the polarization of the pump photons can be changed from vertical to -45° polarization. Then, as SPDC happens, the first crystal produces pairs of horizontally polarized photons from the pump's vertical polarization

¹There is an uncertainty about the exactness of this value, please see Appendix C for the discussions. This dispute is of a minor concern though, as it has rather little effect on the experiment.

component², while the second crystal produces pairs of vertically polarized photons from the pump's horizontal polarization component. With noncollinear SPDC, we set the down-converted photons to travel in different directions with a cone-opening angle of 3° . Note that as the crystals are very thin, and the cone-opening angle is small, the two SPDC cones overlap almost exactly with one another. For our experiment, we shall collect only down-converted photons which travel along the horizontal plane as our two-qubit systems. Since the coherence length of the pump is relatively long, the phase between the horizontally polarized and vertically polarized down-converted photon pairs are always locked together, and thus they are described by

$$|\psi\rangle = \frac{1}{\sqrt{2}}(|H_s H_i\rangle + e^{i\phi}|V_s V_i\rangle), \quad (3.1)$$

where the subscripts s–signal and i–idler (hereafter omitted if no confusion) label the spatial modes. The relative phase ϕ can be tuned by introducing a pair of *quartz plates* in between the HWP and the crystals. By tilting these quartz plates, and hence changing their effective thickness for which the pump is passing across, the ellipticity of the pump's polarization, i.e. the relative phase between its horizontal and vertical components can be manipulated. This change of relative phase is then transferred to the ϕ in Eq.(3.1). As a result, one can prepare the Bell ket $|\Psi^-\rangle = \frac{1}{\sqrt{2}}(|HH\rangle - |VV\rangle)$ ³. Note that if we now change the pump's polarization to 45° by changing the HWP to -22.5° , the ket $|\Psi^+\rangle = \frac{1}{\sqrt{2}}(|HH\rangle + |VV\rangle)$ will be obtained instead.

3.1.2 Rank-1 states

Rank-1 states can be produced from a straightforward generalization of above's methodology and set-up. Instead of setting the HWP at the pump at 22.5° , by turning it to an arbitrary angle $0^\circ \leq \vartheta \leq 90^\circ$, the pump's polarization changes from $|v\rangle \longrightarrow \cos(2\vartheta)|H\rangle - \sin(2\vartheta)|V\rangle$. With SPDC, this generates the states

$$|\rangle_{\vartheta} = \cos(2\vartheta)|HH\rangle - \sin(2\vartheta)|VV\rangle. \quad (3.2)$$

²This is actually a (good) approximation, as the down-converted photons are actually in general not exactly horizontally polarized. For discussions about this issue, please see Appendix C.

³The detailed explanation on checking the correctness of ϕ will be given in Sub.3.3.2.

The purity of this class of states is 1, and the tangle is given by

$$T = \left(1 - \cos(8\vartheta)\right)/2. \quad (3.3)$$

3.1.3 Rank-2 states

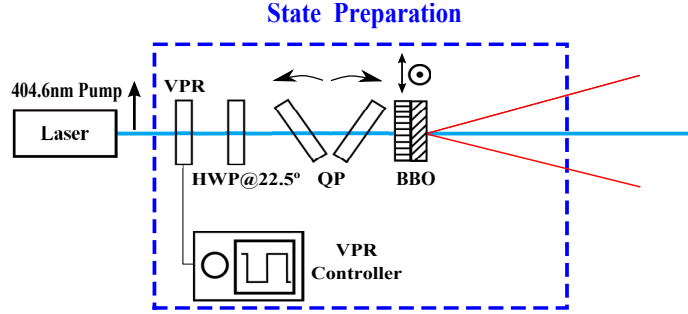


Figure 3.2: Schematic for the generation of rank-2 states. A variable polarization rotator (VPR) is added to the Bell state generation set-up, so that the pump periodically changes between the $+45^\circ$ and -45° polarizations with controlled ratio.

In this project, the basic principle underlying the method of producing rank-2 states is to generate incoherent mixtures of orthogonal Bell states with controllable weights. This can be achieved, by introducing a new piece of instrument, namely a *variable polarization rotator* (VPR), into our previous rank-1 set-up, as depicted in Fig. (3.2).

A VPR is an optical instrument which is able to change the polarization state of the light into *different possible states*, according to some controlled parameters. In our experiment, the VPR used is a *liquid crystal retarder* (LCR) (Meadowlark, LRC-200).

The working principle of a LCR is rather straightforward. By applying electric voltages across, hence changing the alignment of the liquid crystals inside, one obtains an instrument which carries different possible retardances, according to the values of the applied voltage. In particular, one can obtain a half-wave retardance (like a HWP), as well as zero or no retardance at all. However, as introduced in Sec. 2.2.2, whereas a HWP or QWP can be mounted on a rotator to rotate its fast and slow axes at the desired angle θ , our LCR has its fast and slow axes fixed at $\theta = \pm 45^\circ$.

To produce rank-2 states, we put the LCR at just after the laser source, but before a HWP which is rotated at 22.5° , and apply electric voltage in square waveforms

across the LCR. It is configured so that zero retardance is obtained for the low voltage of $V_L = 1.39$ V, and half-wave retardance is obtained for the high voltage of $V_H = 1.64$ V. Then, when zero retardance is achieved, the pump polarization entering the crystals remains at -45° , and $|\Psi^-\rangle$ is generated. When the half-wave retardance is achieved, the pump polarization entering the crystal changes to 45° , and $|\Psi^+\rangle$ is generated. By changing the *duty cycle* (DC) of the square wave, i.e. the ratio of the duration of the high voltage to the period of the waveform, we can thus obtain various blends of the two orthogonal Bell states with controllable weights. That is, we are generating the incoherent mixture

$$\begin{aligned} \rho(\alpha) &= |\Psi^-\rangle(1-\alpha)\langle\Psi^-| + |\Psi^+\rangle\alpha\langle\Psi^+| \\ &= \frac{1}{2}(|\text{HH}\rangle\langle\text{HH}| + |\text{VV}\rangle\langle\text{VV}|) + \left(\alpha - \frac{1}{2}\right)(|\text{HH}\rangle\langle\text{VV}| + |\text{VV}\rangle\langle\text{HH}|), \end{aligned} \quad (3.4)$$

where $\alpha \in [0, 1]$ is equal to the duty cycle. The purity of this class of states is

$$P = 2\left(\alpha - \frac{1}{2}\right)^2 - \frac{1}{2}, \quad (3.5)$$

and the tangle is given by

$$T = \left(1 - 2\alpha\right)^2. \quad (3.6)$$

Of course, to have a meaningful recognition of the states, the period of the square wave must be significantly less than the total time of measurement. In our experiment, the square wave is applied at a frequency of 1 Hz, and the total time of measurement is 1 min for each state.

It is worth mentioning that by using more than one VPR, one can generate rich classes of states. For example, in addition to the above configuration, one can install another similar VPR at the signal arm, and independently control their DCs. If both the DCs are totally uncorrelated and randomized, one obtains the completely mixed state. In contrast, by carefully correlating their DCs, Bell diagonal mixed states, which can be rank-3 or rank-4 states, can be generated. More generally, by rotating the polarization of the pump beam to an arbitrary angle θ , one can obtain mixtures of non-maximally entangled kets $|\Psi_\theta\rangle = \cos(2\theta)|\text{HH}\rangle + \sin(2\theta)|\text{VV}\rangle$. This enables the generation of even more states such as the Collins-Gisin states

[CG04], given by $\rho_{CG} = |\Psi_\theta\rangle\alpha\langle\Psi_\theta| + |\text{HV}\rangle(1-\alpha)\langle\text{HV}|$. Unfortunately, however, due to limitations from our budget and instruments, we regret that these states have not been generated and used for our witness project.

Lastly, we remark that a detailed study on the quality of the rank-2 states $\rho(\alpha)$ in Eq. (3.4), and hence a confirmation on the validity of this method of states generation using VPRs, had been performed. These efforts of introducing a simple and controllable way of generating mixed two-photon states, together with its verification, earned us a publication in the *New Journal of Physics*. We refer the readers to this work [DLT⁺13] for the details.

3.2 Manipulations and control of states

3.2.1 Manipulation & control

As they leave the crystals, the down-converted photons are collected into single-mode optical fibers (SMF) using aspherical lenses with focal length of 11 mm, placed at a distance of about 1050 mm from the BBOs⁴. To compensate or neutralize the changes in polarization accumulated as the photons propagate inside the optical fibers, manual polarization controllers (PCs) are introduced. A PC works by looping the fibers in three consecutive spools of paddles which mimic the function of a QWP-HWP-QWP configuration. These loops produce stress on the fibers which induce effective birefringence on the fibers, where by turning the paddles, one is effectively turning the fast axes of the fibers⁵. After restoring the polarizations, the down-converted photons are out-coupled from the fibers with aspherical lenses of 4.51 mm focal length.

3.2.2 HOM interferometer

Next, we direct the signal and idler photons to interfere at a non-polarizing 50 : 50 BS. The schematic of the set-up is given in Fig. 3.3. As interference effect relies on non-distinguishability of the two parties, the signal and idler photons must reach

⁴See Appendix D for explanation on using this collection distance.

⁵See Appendix D for details on how to use the PCs.

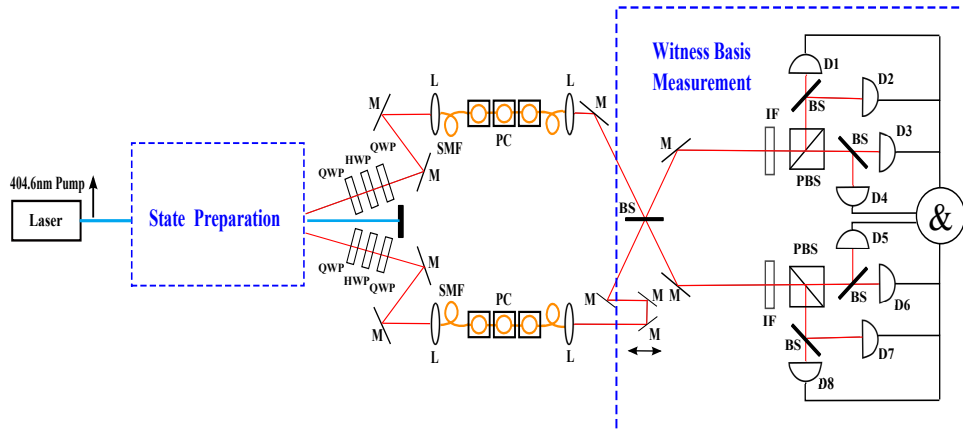


Figure 3.3: From its source, the signal and idlers are collected into SMFs, using lenses (L). Their polarizations are maintained by using the PCs. The photons are directed to interfere at the 50:50 BS, and guided to incident on two PBSs. The IFs are interference filters. Set of wave plates are installed on both arms to perform changes of witness basis. To distinguish the signatures of the four eigenkets of the witness bases, eight detectors are used, and the coincidences between any two detectors are (post-)processed by a coincidence programme (&).

at the same time to, and at the same spot of the BS, within very small margins of errors.

To meet the requirement on their arrival times at the BS, in one arm (say, idler), two mirrors are especially mounted on a motorized stage, which can translate with a minimum step size of $0.5 \mu\text{m}$ (OWIS, Precision Linear Stages Limes 80). The two mirrors are installed such that the photon's incident angles are 45° upon the mirrors, and finally reflects into the reversed direction. This configuration of mirrors is also known as an *optical trombone*. The translation of the linear stage is set in the same axis as the light's incident direction, such that only the distance traveled by the light is altered, but not its path direction.

To make sure that the two light beams overlap well at the beam splitter, after they meet at the BS, we maximize their coupling ratios into a distant SMF. Since coupling into a SMF is very sensitive to minute changes, maximizing the coupling ratios for both arms implies they must have followed (almost) the same path throughout, and originated from the same spot at the BS. In our experiments, we maximize both coupling ratios to about 70%.

3.3 Detection and measurement

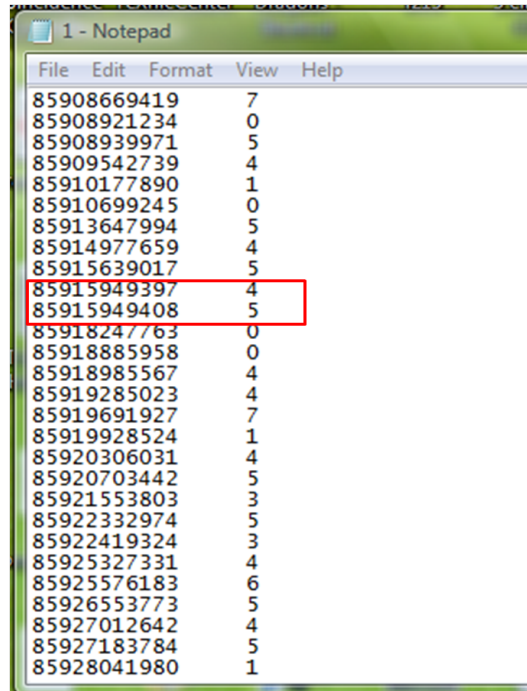
3.3.1 Witness-basis measurement

After their interference at the BS, the two photons are guided to incident on two PBSs, as depicted in Fig. 3.3. Here, the down-converted photons are filtered with interference filters (Andover) centered at 810 nm, with 10 nm full-width-at-half-maximum (FWHM). To obtain the different signatures of the four eigenkets, we need to be able to distinguish and register both one-photon and two-photon events. For this purpose, we introduce four 50:50 BSs at the transmission and reflection ports of the two PBSs. This results in eight output ports in total, which are directed into eight single-photon detectors (Silicon Avalanche Photodiodes, quantum efficiency ~50%, Qtools Twin QuTD), using lenses and multi-mode fibers. This configuration is used because our detectors are not able to distinguish one-photon and two-photon events (they have a dead time of about $1\mu\text{s}$), and hence the signature of $(2,0,0,0)$ for $|\text{HH}\rangle$ in Table 2.2, for instance. By further splitting these two horizontally polarized photons using the 50:50 BSs, we can then detect this signature by registering the *coincidences* between D3-D4, and D5-D6 in Fig. 3.3, and we must not forget to multiply by two to take into account the possibility of two photons going to D3, for example. In our experiment, coincidence events are registered and defined using a (TDC) time-to-digital converter (quTAU, Qtools) with a time window of 5 ns. With this configuration, the signatures of witness-basis measurement in Table 2.2 are now translated to Table 3.1. In reality, we are using four multi-mode fused fiber optics couplers (Thorlabs, FCMM625-50A-FC) as our four 50:50 BSs. Such fibers have one tip where the photons are coupled in, and two other tips where they are coupled out.

Eigenket	Coincidences between the detector pairs
$ \text{HH}\rangle$	$2 \times (\text{D3-D4}), (\text{D5-D6}) \times 2$
$ \text{VV}\rangle$	$2 \times (\text{D1-D2}), (\text{D7-D8}) \times 2$
$ \Phi^+\rangle$	$(\text{D1-D3}), (\text{D1-D4}), (\text{D2-D3}), (\text{D2-D4}),$ $(\text{D5-D7}), (\text{D5-D8}), (\text{D6-D7}), (\text{D6-D8})$
$ \Phi^-\rangle$	$(\text{D1-D5}), (\text{D1-D6}), (\text{D2-D5}), (\text{D2-D6}),$ $(\text{D3-D7}), (\text{D3-D8}), (\text{D4-D7}), (\text{D4-D8})$

Table 3.1: Signatures of measuring the eigenkets of witness operators, using the configuration in Fig. 3.3.

In practice, to evaluate this many coincidences between any two detectors (20 are needed out of 28 in total) in one-go and on the fly using logic electronic circuits, is not feasible. To overcome this, whenever a detector detects a photon and registers a single count, a *timestamp* is assigned to this event. After the experiment is finished, we then collect all these timestamps for all the eight detectors, and post-select the coincidence counts between any two detectors. Coincidences are defined by timestamps which differ by at most 5 ns. Using our TDC above, a resolution of 81 ps for the timestamps can be achieved. A sample of such *click sequence* is shown in Fig. 3.4. Last but not least, we install sets of QWP-HWP-QWP at both signal and idler arms, which are needed to realize all the witness bases in Table 2.1, according to the values given in Eqs. (2.17). Note that they have been installed at before the BS for HOM interference.



Timestamp	Channel Number
85908669419	7
85908921234	0
85908939971	5
85909542739	4
85910177890	1
85910699245	0
85913647994	5
85914977659	4
85915639017	5
85915949397	4
85915949408	5
85918247763	0
85918885958	0
85918985567	4
85919285023	4
85919691927	7
85919928524	1
85920306031	4
85920703442	5
85921553803	3
85922332974	5
85922419324	3
85925327331	4
85925576183	6
85926553773	5
85927012642	4
85927183784	5
85928041980	1

Figure 3.4: An excerpt from the real experimental data for witness basis 1 with the $|\text{HH}\rangle$ ket, where $\vartheta = 90^\circ$ in Eq. (3.2). The left column is the timestamp, where one unit, or *time bin*, corresponds to 81 ps. The time window of 5 ns is then approximated by 62 bins. The right column is the channel number, which corresponds to the detectors shown in Fig. 3.3. Here, we have the mapping of channel numbers to detectors by $0 \leftrightarrow \text{D1}$, $1 \leftrightarrow \text{D2}$, and so on. As an example, there is a coincidence count between D5 and D6 as highlighted above. In our experiments, there are about ten thousand such coincidence counts for each state and each witness basis.

3.3.2 Polarization correlation test

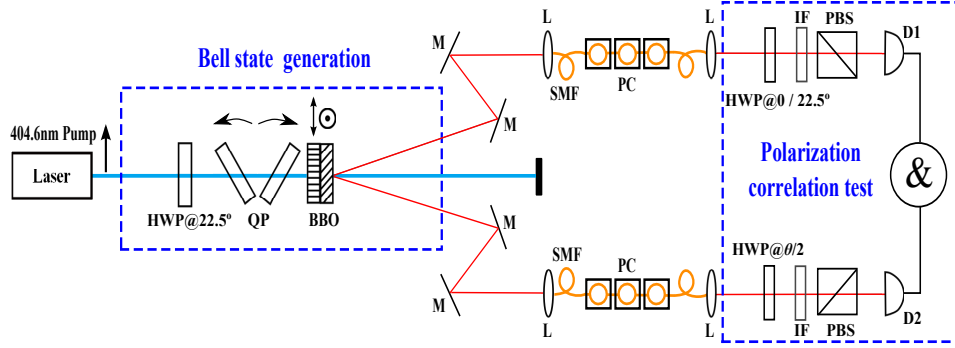


Figure 3.5: Schematic of the experimental set-up for polarization correlation test. Using HWPs and PBSs, polarization correlation tests are performed in two bases, namely the HV basis and $\pm 45^\circ$ basis. D1 and D2 are single-photon detectors, and $\&$ is the coincidence circuit.

Since all our state generations originated from the Bell states, the quality of the Bell states must be insured. To check that the down-converted photons generated, as expected from a Bell state, has a high degree of polarization correlation, *polarization correlation tests* are performed. At one arm (say, signal), the HWP is fixed at 0° or 22.5° for analysis in the HV basis or $\pm 45^\circ$ basis respectively, while the HWP at the other arm (idler) is rotated by angle $\theta/2$. Both HWPs are followed by a PBS, and the light that passes through the transmitted ports of the PBSs shall be collected by two single-photon detectors, see Fig. 3.5. The *coincidence rates* between the counts of the two single-photon detectors are then recorded. That is, we are probing the values of $\text{tr}\{\rho | \rangle \langle | \}$, where $| \rangle = |H_s\rangle(\cos(\theta)|H_i\rangle + \sin(\theta)|V_i\rangle)$ or $|+45_s^\circ\rangle(\cos(\theta)|H_i\rangle + \sin(\theta)|V_i\rangle)$. Here, the coincidence events, defined by time window of 5 ns, are evaluated on the fly, using our TDC.

A measure of polarization correlation is the *visibility*, defined as

$$V = \left| \frac{N_{0^\circ} - N_{90^\circ}}{N_{0^\circ} + N_{90^\circ}} \right| \quad (3.7)$$

for measurement in the HV basis, or

$$V = \left| \frac{N_{+45^\circ} - N_{-45^\circ}}{N_{+45^\circ} + N_{-45^\circ}} \right| \quad (3.8)$$

for measurement in the $\pm 45^\circ$ basis. Here, N_θ is the coincidence rate when the HWP in the idler arm is oriented at $\theta/2$. Our experimental results with $\rho = |\Psi^+\rangle\langle\Psi^+|$ are shown in Fig. 3.6. High visibilities ($98.1 \pm 1.4\%$ and $97.3 \pm 1.4\%$ respectively) in both the HV and $\pm 45^\circ$ bases indicate high quality of the produced Bell state.

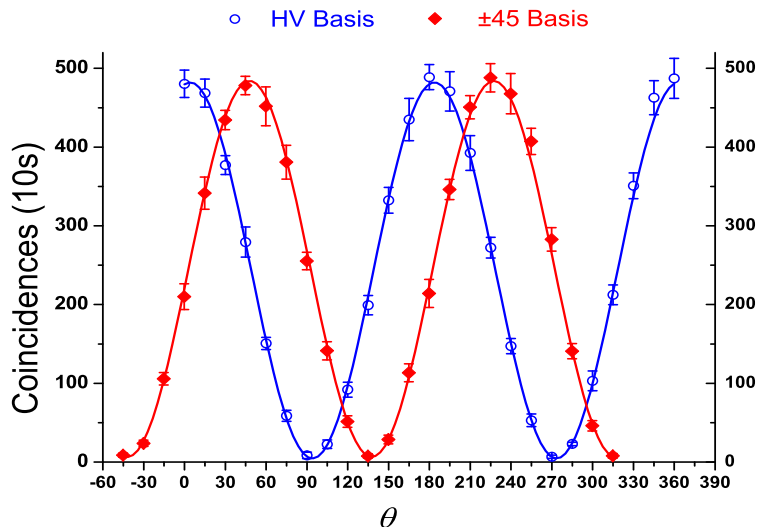


Figure 3.6: Polarization correlation analyses, for the Bell ket $|\Psi^+\rangle$. The tests show strong polarization correlation between the down-converted photons which is independent of the measurement basis, and hence a confirmation of the highly-entangled source. Not shown are the single counts of the two detectors, which are both about 22,000 counts per ten seconds, and are almost not modulated by θ .

3.3.3 Characterization of HOM interferometer

The quality of the HOM interferometer is equally important in this experiment. To check it, we first prepare the photons in the ket $|\text{HH}\rangle$, and remove the two BSs in front of the detectors D3, D6. Then, by translating the motorized stage in the idler arm, and thus changing the differences in the photons' arrival times at the beam splitter, we obtain the so-called HOM *dip*, shown in Fig. 3.7. It plots the number of coincidence rates between D3-D6 as a function of the stage position.

Quantitatively, we define the dip *visibility*, V as

$$V = \frac{N_{\max} - N_{\min}}{N_{\max} + N_{\min}}, \quad (3.9)$$

where N_{\max} is the maximum coincidence rates at asymptote, and N_{\min} is the mini-

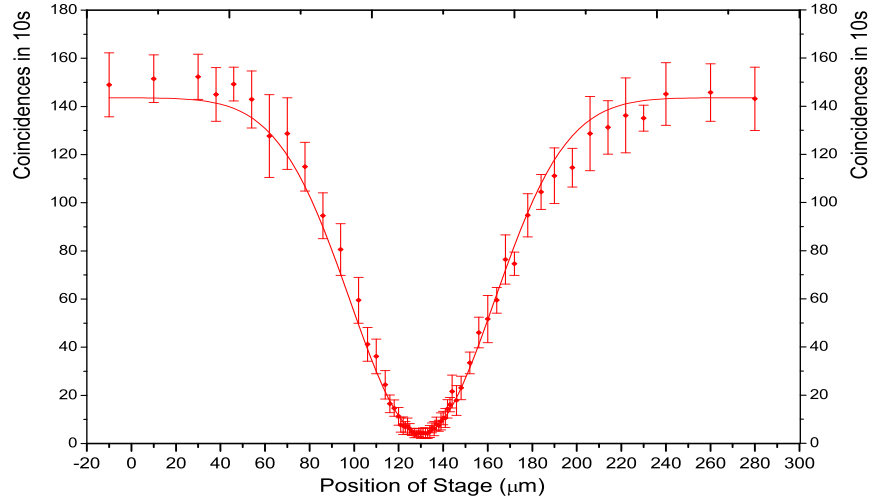


Figure 3.7: The HOM dip. The stage position at around $130 \mu\text{m}$ indicates almost equal detection time for the photons, making them indistinguishable in principle. A sharp decrease in the coincidence rates is thus observed, as the stage translates along. The smooth curve is a fitted Gaussian, which corresponds to interference filters with Gaussian profile.

mum coincidences rates at the dip. For the HOM dip above, the visibility obtained is $94.5 \pm 11.2\%$. This indicates that we have established a reliable interferometer.⁶

Two remarks about the stability of HOM interferometer are in order: Firstly, the *width* of the HOM dip is proportional to the coherence length of the SPDC photons. Since SPDC is possible for non-degenerate wavelengths, the SPDC spectra are usually quite broad, which results in very short coherence length. This is the reason why interference filters are needed, apart from filtering stray photons. The IFs effectively increase the coherence length of the SPDC photons by narrowing the SPDC spectra. A wider dip provides more robustness to interferometric instability, provided the disturbance is not too large. It also increases the overlap of the two dips from the two crystals.

Thus, we need to identify any disturbance that induces interferometric instability, and kept them minimal for at least the duration that is needed for our experiment. In our experiment, we found that the air flow from the air-condition has brought

⁶Correspondingly, for the ket $|\nu\nu\rangle$, we have a second dip. As their origins are two different crystals, the dips are very close, but not exactly overlapping.

significant instability to the HOM dip. By covering the set-up with hardboards, we are then able to obtain a stable HOM dip for duration of at least ten minutes. The result of this simple stability check is reproduced in the figure below.

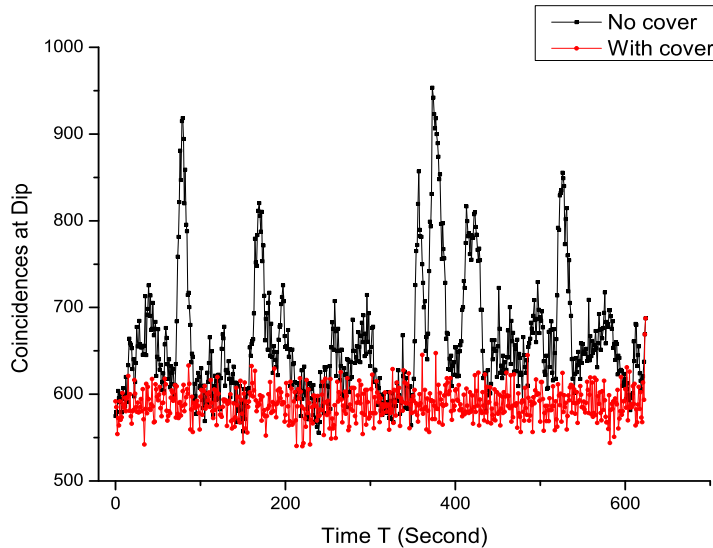


Figure 3.8: The coincidence counts at the HOM dip for ten minutes, both with cover (red), and without cover (black). To observe the instability more clearly, the above results were obtained without interference filters. Here, the maximum coincidence rates N_{\max} is around 2000 counts per second.

3.3.4 Detector calibration

Detector efficiency

It was assumed implicitly that the detectors are perfect in our discussions in the previous sections. However, in real experiments, all detectors have detection efficiencies. For a detector with efficiency 50%, this means half the time, it will miss a detection, even when the photons are not reaching within its dead time. Here, we shall not be concerned with the physical reasons behind such detection inefficiencies, but rather, their consequences. In our experiment, we are using eight detectors, where all of them have their own efficiencies. If these discrepancies are to be ignored, wrong statistics will be obtained. To take this into account, we introduce a renormalization to the statistics registered, such that the results obtained, after these corrections, will reflect the true statistics, i.e. as if the detectors had equal

efficiencies.

To do this, right before (or right after) the experiment, we calibrate the detector efficiencies, by using the same, stable photon source. That is, by using a same photon source, the number of photons, N_k , registered by each detector D_k , are recorded. Then, the detector which gives the largest count, say $N_{k'}$, will have its efficiency normalized to 1. All other detectors will then have their relative efficiencies given by $\eta_k = N_k/N_{k'}$. To renormalize the statistics, for every N_k photons detected by D_k , we divide by η_k , to include the missing detections. This correction scheme works similarly for coincidence events. For example, suppose D3 and D4 registered N coincidences, then we renormalize it to $N/(\eta_3\eta_4)$.

Single counts

Another type of correction to the statistics is known as the elimination of *accidental coincidences*. Accidental coincidences are coincidence events that come from photons which are not conjugate pairs of the SPDC, but perhaps some stray photons, or the minimum background count of the detectors (which is on average about 700, typically). Evidently, the larger the single counts of the two detectors, the larger the possibility of registering such accidental coincidences. Quantitatively, the accidental coincidence rates are estimated by

$$\Delta n = \frac{N_j}{\eta_j} \times \frac{N_k}{\eta_k} \times \Delta t, \quad (3.10)$$

where N_j/η_j and N_k/η_k are the respective renormalized single count rates of the two detectors of interest, and Δt is the time window defining the coincidence events. As a concrete example, in our experiment, $\Delta t = 5$ ns and $N_j, N_k \approx 2000$ Hz, telling us $\Delta n \approx 0.05$ Hz, which is a rather small correction.

3.4 Rank-4 states

The kind of rank-4 states that we are generating is known as the Werner states [Wer89]:

$$\rho(\lambda) = |\Phi^-\rangle\lambda\langle\Phi^-| + (1-\lambda)\frac{\mathbb{1}}{4}. \quad (3.11)$$

It can be thought as mixtures of the singlet Bell state with the unpolarized light, or the completely mixed state, in the proportion of $\lambda : (1 - \lambda)$. The purity of this class of states is

$$P = \frac{1}{4}(1 + 3\lambda^2), \quad (3.12)$$

and the tangle is given by

$$T = \left(\frac{3\lambda - 1}{2}\right)^2 \eta\left(\lambda - \frac{1}{3}\right), \quad (3.13)$$

where $\eta(\cdot)$ is the Heaviside unit step function.

Due to lack of instruments, our rank-4 states are not generated in a direct manner, as compared to the previous two classes of states. Instead, we first look at the expected statistics of polarization correlation test and witness-basis measurement using the Werner states.

3.4.1 Expected statistics

Bell component:

As a first step, observe that polarization correlation test performed in the $\pm 45^\circ$ determines λ experimentally. The visibility, according to Eq. (3.8), is

$$V = \left| \frac{\frac{\lambda}{2}}{\frac{\lambda}{2} + \frac{1-\lambda}{2}} \right| = \lambda. \quad (3.14)$$

Note that if there are N copies of the Werner states, which can be thought as mixtures of $N\lambda$ copies of the singlet Bell state and $N(1 - \lambda)$ copies of the completely mixed state, $\{N_{+45^\circ}, N_{-45^\circ}\}$ for these two components, separately, are $\{0, N\lambda/2\}$ and $\{N(1 - \lambda)/4, N(1 - \lambda)/4\}$.

$\frac{1}{4}$ component:

Now, if we perform our measurement with witness basis 1, for the $|\Phi^-\rangle$ component, we expect $N\lambda/8$ coincidences registered for each of the eight detector pairs for eigenket $|\Phi^-\rangle$ in Table 3.1, and no counts for the other three eigenkets. For the

completely mixed state component, we expect $N(1 - \lambda)/4$ coincidences for each of the *signatures*. That is, we expect $N(1 - \lambda)/16$ coincidences for each of the detector pairs for $|\text{HH}\rangle$ and $|\text{VV}\rangle$ eigenkets (which needs to be multiplied by two later), and $N(1 - \lambda)/32$ for each of the sixteen detector pairs for $|\Phi^+\rangle$ and $|\Phi^-\rangle$ eigenkets.

3.4.2 Generating Werner states

To generate the Werner states *experimentally*, we now briefly review the methodology adopted from reference [LHLLK06]. First, produce the Bell ket $|\Psi^-\rangle = \frac{1}{\sqrt{2}}(|\text{HH}\rangle - |\text{VV}\rangle)$, using the method discussed in Sec. 3.1.1. Then, by installing a HWP at 45° in the signal arm, we obtain the Bell ket $|\Phi^-\rangle$. Next, by introducing a very weak laser source which is coupled to two collimators using a fused fiber, we intentionally introduce additional photons to all the detectors, through the unused port of the two PBSs in Fig. 3.3. They are added very carefully such that the total registered single counts (i.e. without efficiencies correction) for each of the eight detectors are roughly the same. Typically, before these additional photons are included, the single counts for the detectors are about 2000 per second. In our experiment, we add these additional photons such that the single count rates are about 4000 Hz for each detector.

Bell component:

We first perform polarization correlation test, which also serves as a good check for the quality of our singlet Bell state. Here, we differentiate the raw coincidence counts from those of post-(detector efficiencies and accidental coincidence corrections) with N^r and N^c . We also modify the convention from previous sections, such as writing $N^c(+45^\circ)$, instead of $N^c_{+45^\circ}$. In particular, for quantities that only refer to the Bell state component, we provide a subscript $_b$.

The visibility for our Bell state is then

$$V = \left| \frac{N_b^c(+45^\circ) - N_b^c(-45^\circ)}{N_b^c(+45^\circ) + N_b^c(-45^\circ)} \right|. \quad (3.15)$$

The single counts for the two detectors, which are about 4000 Hz as mentioned, are also recorded; we shall label them as N'_1 and N'_2 .

$\frac{1}{4}$ component:

Now, we increase the time window defining the coincidence events to Δt_2 , say, 100 ns. Then, the component that is purely related to the accidental coincidences can be obtained as $N^r - N_b^r \equiv N_{\mathbb{1}}$. Note that according to Eq. (3.10), if N'_1 and N'_2 are multiplied by γ'_1 and γ'_2 respectively, $N_{\mathbb{1}}$ will then be $\gamma'_1\gamma'_2 N_{\mathbb{1}}$. The visibility, V , which will determine the parameter λ of our Werner states experimentally, is then given by (assuming now there is a need for γ'_1 and γ'_2)

$$V = \lambda = \frac{N_{\max} - N_{\min}}{N_{\max} + N_{\min}}, \quad (3.16)$$

where $N_{\max} = N_b^c(-45^\circ) + \gamma'_1\gamma'_2 N_{\mathbb{1}}(-45^\circ)$, and $N_{\min} = N_b^c(+45^\circ) + \gamma'_1\gamma'_2 N_{\mathbb{1}}(+45^\circ)$. In essence, to obtain various λ , and hence different Werner states, we just need to apply different time windows Δt to include appropriate amount of accidental coincidences to the detector pairs.

3.4.3 Link to witness-basis measurement

To extend and apply the methodology above to our experiment, we must carefully conserve and map all the relation between the statistics of polarization correlation test to the ones of the witness-basis measurement, according to Sec. 3.4.1 above. Of course, when performing the witness-basis measurement, the set-up for the additional photons and the detectors are left untouched as above.

Bell component:

For the singlet Bell state, i.e. when $\Delta t = 5$ ns, we record down the coincidences between the detector pairs as summarized in Table 3.1. Of course, for any detector pairs $Dj-Dk$, first there is the raw coincidence counts with the label $N_b^r(j, k)$, and then there is the corrections discussed in Sec. 3.3.4, giving us the new count $N_b^c(j, k)$. The sum of the corrected counts for the four eigenket signatures then gives us the total number of biqubits; we can also estimate this number by taking the average of the sum for the six different witness bases. This sum, ideally, must tally with $N_{b, \text{total}} \equiv 2 \times (N_b^c(-45^\circ) + N_b^c(+45^\circ))$ above. Realistically, in our experiment, some losses are unavoidable, and we have only about 60% of $N_{b, \text{total}}$ for our witness-family

measurements. Hence, consciously aware of these losses, we multiply all the counts of the four signatures by a factor of about 5/3, and label them as $N_{\text{h}}^{\text{c}}, N_{\text{v}}^{\text{c}}, N_{+}^{\text{c}}, N_{-}^{\text{c}}$, respectively.

$\frac{\mathbb{1}}{4}$ component:

We now extend Δt beyond 5ns. As before, we obtain first the raw coincidence counts of the detector pairs, $N^{\text{r}}(j, k)$. To single out the completely mixed state component, we minus away all the raw coincidence counts for the Bell state component, i.e. $N^{\text{r}}(j, k) - N_{\text{b}}^{\text{r}}(j, k) \equiv N_{\mathbb{1}}(j, k)$. Since ideally, for the completely mixed state, all the detector pairs should share same amount of coincidences (except those responsible for the product eigenkets which differ by a factor of two), see Sec, 3.4.1, we normalize the single counts N_1, N_2, \dots according to a chosen one, say $N_{k'}$. Also, we must not forget that the sum of $N_{\mathbb{1}}(j, k)$ for all pairs should ideally tally with $4\gamma_1'\gamma_2'N_{\mathbb{1}}$ obtained from the polarization correlation test, where $\gamma_1' \equiv N_1'/N_{k'}$, $\gamma_2' \equiv N_2'/N_{k'}$. Then, with $\gamma_j \equiv N_k/N_{k'}$, we have $N_{\mathbb{1}}(j, k) \rightarrow \frac{\gamma_j\gamma_k N_{\mathbb{1}}(j, k)}{8}$ for the (j, k) pairs that measures the two Bell eigenkets, and $N_{\mathbb{1}}(j, k) \rightarrow \frac{\gamma_j\gamma_k N_{\mathbb{1}}(j, k)}{4}$ for the (j, k) pairs that measures the two product eigenkets. We remind the readers not to confuse γ_j with η_j , where the latter is the detector efficiency.

Finally, the full witness measurement result for a Werner state is the addition of the counts from the singlet Bell state component, with the counts from the completely mixed state component. As an example, for the signature of the eigenket $|\text{HH}\rangle$, the total coincidence counts are

$$N_{\text{h}} = N_{\text{h}}^{\text{c}} + 2 \times \frac{\gamma_3\gamma_4 N_{\mathbb{1}}(3, 4)}{4} + 2 \times \frac{\gamma_5\gamma_6 N_{\mathbb{1}}(5, 6)}{4}. \quad (3.17)$$

3.5 A discussion: How the experiment is actually performed

With all these individual pieces about the experiment and its implementation explained, we are now ready to discuss an important point on the actual procedure in running the experiment. In reality, the experiment is done with the following steps:

1. First, prepare the quantum states.
2. Perform witness-family measurements. For each state, always perform measurements in *all* the six bases, and record down the frequencies and sequences for each of the detector clicks for each basis.
3. With the measurement results of all the six bases available at hand, we start with randomly analyzing one of the basis. The evaluation then follows the two adaptive schemes highlighted in Sec. 2.1.3, to determine if the state is entangled. Repeat this for all states measured.

The reason why we always measure all the six bases and perform the analysis afterwards, but not performing a real time entanglement detection which stops as soon as the state is determined as entangled, is twofold. Firstly, the measurement results of these six bases, which form an IC POM, allow us to reconstruct the state by using ML estimation. This allows us to check, for consistency, that we are generating the intended states with high precisions or fidelities. The second reason is, with all these results of different bases available, we can perform data manipulations and analyses in a much convenient way. For example, for a same state, we do not need to do the experiment six different times. Rather, we just analyze the results we had, by choosing different starting basis. All these data also allow us to perform error analysis by using various statistical techniques, which will be covered in the next chapter.

Chapter 4

Results

In this chapter, we include the results for (i) the fidelities of the generated states, (ii) witness-family measurements, and (iii) error analyses.

4.1 Fidelities

As mentioned in the previous chapter, we adopt the strategy of always performing IC measurements followed with post-entanglement detections, such that we can check on the quality of the generated states, through ML state estimation technique. All bases are measured for one minute, which corresponds to qubit copies of about 10,000.

4.1.1 Rank-1 states

For rank-1 states, we generated 21 states from the class of

$$|\rangle_{\vartheta} = \cos(2\vartheta)|HH\rangle - \sin(2\vartheta)|VV\rangle, \quad (4.1)$$

with tangle given by Eq. (3.3).

The fidelities of the ML estimators with the target states, as well as their purities and tangles, are summarized in Table 4.1. Note that the fidelities are smaller than 99.4%, which is consistent with the limit given by the Migdall effect, as discussed in Appendix C. Plot of tangle of the ML estimators are illustrated in Fig. 4.1.

ϑ (degree)	Purity	Fidelity	Tangle (Theory)	Tangle (Experiment)
0 $ \text{HH}\rangle$	0.990	0.988	0	0.008
5	0.981	0.987	0.117	0.108
10	0.963	0.983	0.420	0.336
15	0.973	0.978	0.750	0.656
20	0.959	0.981	0.970	0.865
22.5 $ \Psi^-\rangle$	0.943	0.976	1.000	0.880
25	0.922	0.971	0.970	0.839
30	0.922	0.966	0.750	0.654
35	0.931	0.974	0.420	0.326
40	0.967	0.986	0.117	0.070
45 $ \text{VV}\rangle$	0.983	0.992	0.000	0.004
50	0.945	0.983	0.117	0.147
55	0.919	0.974	0.420	0.378
60	0.918	0.957	0.750	0.726
65	0.946	0.959	0.970	0.885
67.5 $ \Psi^+\rangle$	0.951	0.976	1.000	0.882
70	0.970	0.983	0.970	0.848
75	0.955	0.975	0.750	0.630
80	0.966	0.982	0.420	0.333
85	0.979	0.987	0.117	0.091
90 $ \text{HH}\rangle$	0.984	0.989	0.000	0.001

Table 4.1: Rank-1 states: Fidelities of the ML estimators with the target states given by Eq. (4.1) are computed. The tangles of the ML estimators are also compared with the expected value of Eq. (3.3). The purity of the ML estimators are also included; theoretically, they should be one.

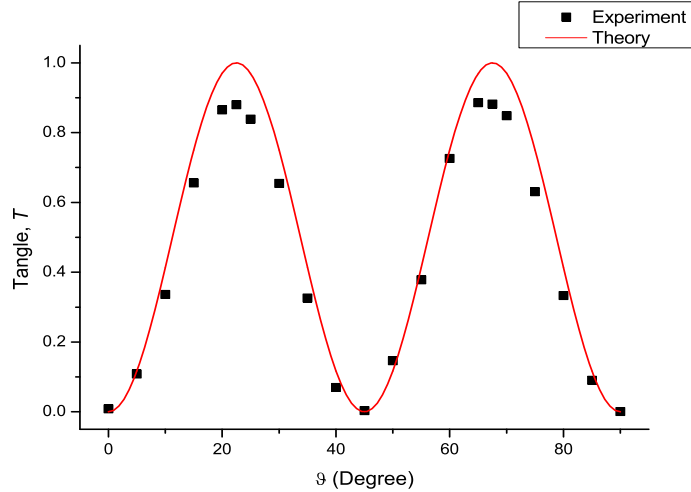


Figure 4.1: Plot of tangle of the ML estimators, compared with the theoretical curve given by Eq. (3.3). The error bars are smaller than the symbols used.

4.1.2 Rank-2 states

For rank-2 states, we generated 21 states from the class of

$$\rho(\alpha) = |\Psi^-\rangle(1 - \alpha)\langle\Psi^-| + |\Psi^+\rangle\alpha\langle\Psi^+|. \quad (4.2)$$

The purity and tangle are given by Eq. (3.5) and Eq. (3.6), respectively.

The fidelities of the ML estimators with the target states, as well as their purities and tangles, are summarized in Table 4.2. As above, the fidelities are smaller than 99.4%. Plots of purity and tangle of the ML estimators are illustrated in Fig. 4.2.

α	Purity (Th)	Purity (Ep)	Fidelity	Tangle (Th)	Tangle (Ep)
0 $ \Psi^-\rangle$	1	0.943	0.976	1.000	0.880
5	0.905	0.864	0.945	0.810	0.729
10	0.82	0.821	0.933	0.640	0.623
15	0.745	0.700	0.960	0.490	0.407
20	0.68	0.670	0.952	0.360	0.336
25	0.625	0.606	0.978	0.250	0.213
30	0.58	0.586	0.965	0.160	0.165
35	0.545	0.555	0.974	0.090	0.112
40	0.52	0.524	0.975	0.040	0.058
45	0.505	0.513	0.980	0.010	0.029
50	0.5	0.516	0.986	0.000	0.029
55	0.505	0.529	0.980	0.010	0.043
60	0.52	0.543	0.983	0.040	0.055
65	0.545	0.575	0.985	0.090	0.113
70	0.58	0.596	0.985	0.160	0.161
75	0.625	0.636	0.989	0.250	0.251
80	0.68	0.686	0.979	0.360	0.336
85	0.745	0.734	0.973	0.490	0.408
90	0.82	0.840	0.964	0.640	0.601
95	0.905	0.878	0.982	0.810	0.707
100 $ \Psi^+\rangle$	1	0.951	0.976	1.000	0.882

Table 4.2: Rank-2 states: Fidelities of the ML estimators with the target states given by Eq. (4.2) are computed. The tangles of the ML estimators (Ep) are also compared with the expected value of Eq. (3.6) (Th). The purities of the ML estimators are also included; they are to be compared with Eq. (3.5).

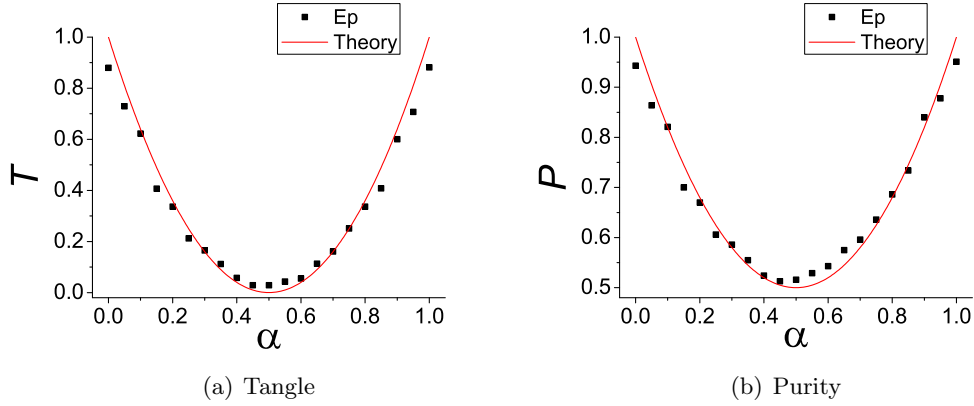


Figure 4.2: Plots of tangle and purity of the ML estimators, compared with the theoretical curves given by Eq. (3.6) and Eq. (3.5) respectively. The error bars are smaller than the symbols used.

4.1.3 Rank-4 states

For rank-4 states, we generated 22 states from the class of

$$\rho(\lambda) = |\Phi^-\rangle\lambda\langle\Phi^-| + (1 - \lambda)\frac{\mathbb{1}}{4}. \quad (4.3)$$

The purity and tangle are given by Eq. (3.12) and Eq. (3.13), respectively.

The fidelities of the ML estimators with the target states, as well as their purities and tangles, are summarized in Table 4.3. To confess a point, we have ‘normalized’ the state with time window $\Delta t = 5$ ns as our Bell ket $|\Phi^-\rangle$ (see discussion in Sec. 3.4). This is, of course, an idealization, since one would never measure a visibility of 1 in experiment (even after deducting all accidental counts). The measured visibility was actually 97.7%, with the corresponding tangle $T \approx 0.932$.

Notice that as the weight of the white noise dominates, the fidelity increases beyond 99.1%. In fact, as we increase the time window, the number of copies of the Bell state remains at about 10,000, while the qubit pairs from the white noise increases to about 6,000 for $\Delta t = 5000$ ns. This reduction in contribution from systematic error as the λ decreases from one to $\frac{1}{3}$ is also well captured in the plot of purity and tangle shown in Fig. 4.3.

Δt (ns)	λ	Purity(Th)	Purity(Ep)	Fidelity	Tangle(Th)	Tangle(Ep)
5 $ \Phi^-\rangle$	1	0.965	0.870	0.959	1	0.760
50	0.960	0.941	0.846	0.977	0.882	0.707
100	0.939	0.912	0.821	0.976	0.826	0.656
250	0.883	0.834	0.761	0.971	0.679	0.540
500	0.804	0.734	0.687	0.964	0.498	0.403
750	0.741	0.662	0.627	0.975	0.375	0.305
1000	0.681	0.598	0.574	0.984	0.272	0.226
1250	0.631	0.549	0.532	0.988	0.200	0.167
1500	0.587	0.508	0.498	0.990	0.145	0.124
1750	0.551	0.477	0.470	0.992	0.106	0.091
2000	0.516	0.450	0.447	0.993	0.075	0.067
2250	0.485	0.426	0.426	0.994	0.052	0.047
2500	0.456	0.406	0.410	0.995	0.034	0.033
2750	0.433	0.390	0.395	0.995	0.022	0.023
3000	0.411	0.377	0.382	0.996	0.014	0.015
3250	0.390	0.364	0.372	0.996	0.007	0.009
3500	0.372	0.354	0.362	0.996	0.003	0.005
3750	0.357	0.346	0.354	0.997	0.001	0.003
4000	0.342	0.338	0.347	0.997	0.0002	0.001
4250	0.327	0.330	0.340	0.997	0	0.0001
4500	0.316	0.325	0.334	0.997	0	0
5000	0.292	0.314	0.324	0.998	0	0

Table 4.3: Rank-4 states: Fidelities of the ML estimators with the target states given by Eq. (4.3) are computed. The tangle of the ML estimators (Ep) are also compared with the expected value of Eq. (3.13) (Th). The purity of the ML estimators are also included; they are to be compared with Eq. (3.12). The last two states are not used for testing the witness-family measurements.

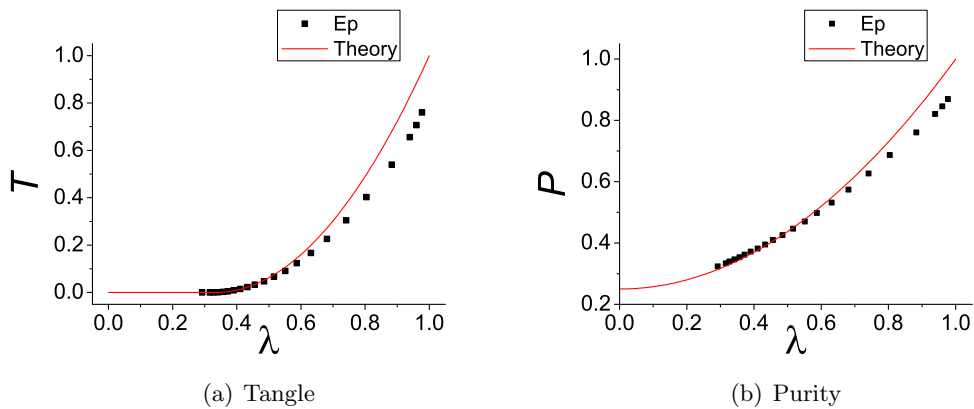


Figure 4.3: Plots of tangle and purity of the ML estimators, compared with the theoretical curves given by Eq. (3.13) and Eq. (3.12) respectively. The error bars are smaller than the symbols used.

4.2 Simulation results

There are infinitely many quantum states in the state space, but there are limited resources in our experiment. Hence, before focusing on the experiment results that we have, we use computer simulations to study the *general* performance of the witness-family measurements for *general* states.

To be specific, we perform computer simulations for *arbitrary* rank-1 and rank-4 states. For each of these two classes, we randomly generated 10,000 states, and then perform the simulated witness-family measurements. To summarize the performance of the witness-family measurements, we plot the cumulative histogram of number of states detected, as the number of witnesses needed increases. In accordance with our theoretical prediction, in the order of schemes A to B to C, the histogram should show largest, smaller, and smallest average number of witnesses needed to detect the states.

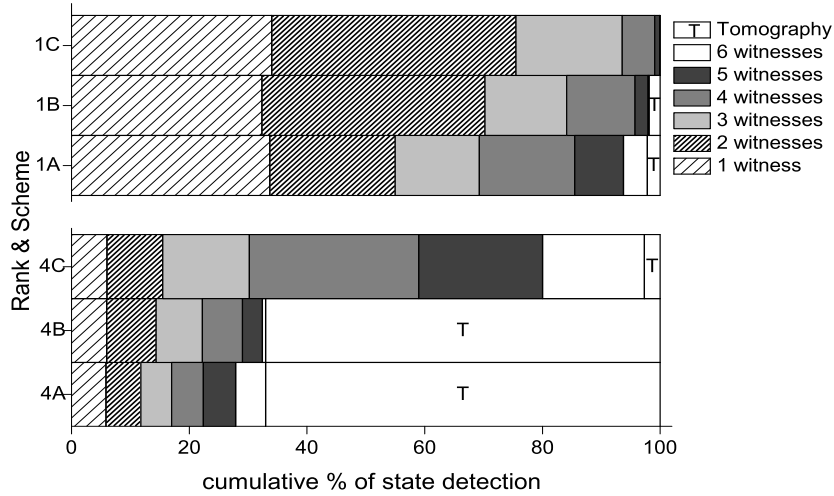


Figure 4.4: Cumulative histograms showing the number of witnesses needed to detect 10,000 states, using various schemes proposed in Sec. 2.1 As a general trend, scheme C gives the best performance, followed by scheme B and A. Note that scheme C not only reduces the average witnesses needed, but it also increases the number of states detectable without performing quantum state tomography.

The simulation results, shown in Fig. 4.4, confirms our prediction.¹ For rank-1 states and rank-4 states, using scheme A or B, about 2% and 67% of the states

¹These results were actually reproduced from Yong Siah Teo's PhD thesis [Teo13], where the original results were presented separately in ordinary histograms rather than cumulative histograms.

are undetected by the six witness bases without performing the full quantum state tomography. With scheme C which introduced the additional step of separability check, the percentage of undetected pure states is reduced to practically zero and one needs no more than five witness bases to detect entanglement for the rest of the pure states. The improvement is even more dramatic for the mixed states, with a reduction from about 67% to 2.7%. Another observation is, the mean number of witness bases needed to detect entanglement for mixed states is higher than that for pure states. This is not surprising, since mixed states generally have lower entanglement and are, therefore, harder to detect.

4.3 Experimental results

For the specific classes of states that we generate experimentally, similar histograms can be plotted, too. To make fair comparison with the experimental results, we simulate randomly 10,000 states from *exactly* these three classes of states. For direct comparison, we present the results in the form of *non-cumulative* histograms, where the experimental and simulation results are put side-by-side.

The histogram results are shown in Fig.4.5. Unshaded histograms are simulated results, while shaded histograms are experimental results. For the first row, i.e. histograms (a) and (d), we have results for rank-1 states. Similarly, the second and third row show the results for rank-2 and rank-4 states, respectively. Meanwhile, the first column, i.e. histograms (a), (b) and (c) summarizes the results obtained by using scheme B, while the second column summarizes the results for scheme C. Not shown here are the histograms summarizing the results for detection scheme A, i.e. detection scheme with randomized settings. For the three classes of states we are considering, such histograms are the trivial ones: Since there is only one basis that can detect entanglement by violating the inequality Eq.(2.3)², with a non-adaptive and randomized settings, we will get a constant or flat histogram, with equal probability of 1/6 for any number of witness needed.

As clearly illustrated by the histograms, we can see that the adaptive Scheme C generally reduces the average number of witnesses needed to detect the states.

²For rank-1 and rank-2 states, it is witness basis 2, while for rank-4 states, it is witness basis 1.

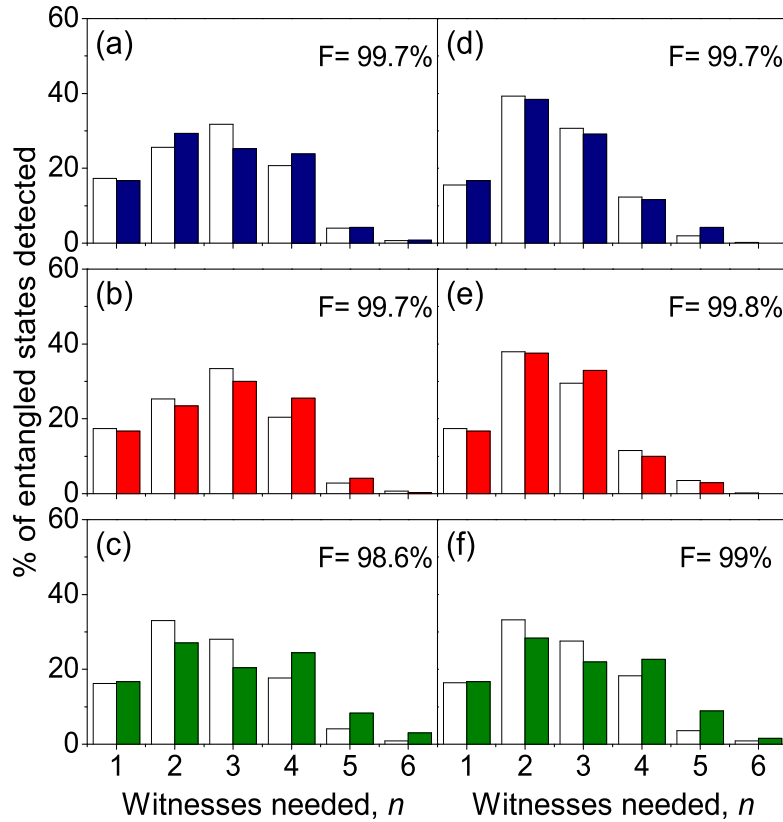


Figure 4.5: Histograms of percentage of states detected versus the number of witnesses needed. For both simulations (unshaded) and experimental (shaded) results, the number of states are about 10,000. The first row, i.e. (a) and (d), shows the results for rank-1 states. Similarly, the second and third row show the results for rank-2 and rank-4 states respectively. The first column, i.e. histograms (a), (b) and (c) summarizes the results obtained by using scheme B, while the second column summarizes the results with scheme C. The high fidelities ($\approx 99\%$) of the histograms show that the experimental and simulation results agree very well.

Qualitatively, we see very positive results, where the simulation and experimental histograms are indeed very similar. To be more precise, we calculate the *fidelity* between the experimental histograms with their corresponding simulation histograms. By definition, given two distributions, say $\{p_i\}$ and $\{q_i\}$ where $\sum_i p_i = \sum_i q_i = 1$, their fidelity, which is given by $F = \sum_i \sqrt{p_i q_i}$, is a popular measure of the “closeness” between two distributions. If the two distributions are identical, $F = 1$; if there is no overlap between them, $F = 0$. For our experimental and simulation results, we obtain high fidelities ($\approx 99\%$) between the simulation and experimental histograms, which means our experimental results agree very well with the simulation results.

4.4 Statistical analysis: Bootstrapping

The histograms shown above are obtained by starting the measurement with a randomly chosen witness basis, for each of the states. Inevitably then, if we re-run our measurements, we are very likely to obtain another set of histograms that is not identical with the above one, even if we are using exactly the same states and the same measured frequencies. In general, how would this randomness in initializing our bases measurement affect the trend of the histograms?

Practically, there are limitations in real experiments. As we have discussed in the previous chapter, there are many sources of errors in our experiment, including imperfections of the states or the measurements, as well as finiteness of the state sampling size. These give rise to small deviations or fluctuations to the measured frequencies, as compared to the ideal situations. Hence, even if we were to repeat the experiment for many times, we are very likely to obtain different values of measured frequencies, which scattered around their mean values. Of course, we have tried to minimize our experimental errors so that they have been kept at a minimum level, so that we are quite positive that our witness-family measurements schemes are quite robust to small errors of such— as can be seen from the results in Fig. 4.5 and their fidelities— such deviations or fluctuations in the data should still not be forgotten.

To complete our understanding about the performance of our witness-family measurements protocol, we thus need to include a quantitative analysis on the effect of random starting basis, with fluctuations in statistics included. In a verbatim way, we would like to now “add error bars” to the histograms shown in Fig. 4.5. The most natural and fair way to produce such error bars is to repeat the experiments for each state for many times. Then, we can average over all such ensembles to obtain a mean fidelity, and also the standard deviation. However, such approach would take us a very long time to collect enough data that are statistically representable. Hence, this method is ruled out for practical purposes.

Since the effect of random starting basis and data fluctuations on the histograms are propagated through complicated numerical calculations of MLME estimators and numerical searches over state space to obtain the likelihood (for Scheme C), estimat-

ing the error bars through a parametric way is almost immediately impossible. To solve this issue, we shall utilize a non-parametric statistical analysis method known as the *bootstrapping* technique [Che99, Dav97]. To apply this technique, let us first extract all the *coincidences sequence* from the click sequence shown in Fig. 3.4, and then label them from 1 to N , according to their timestamps. Then, by using a (pseudo-)random number generator, we generate N numbers with values from 1 to N randomly assigned to them. Note that these values are randomly assigned and repeated indices are therefore allowed. In essence, we are generating a *bootstrap sequence*: A random sequence, weighted by a prior sequence, which is, in our case, the experimental coincidence sequence. Finally, by picking the coincidences *according to* this bootstrap sequence, we obtain a new sequence of coincidences count. By construction, it is in general different from the original one, but there is no intended bias from the original coincidence sequence.

For our experiment, with our state sample size as large as 10,000 copies, we generate one hundred bootstrap sequences. Then, each of these bootstrap sequence gives us a histogram similar to Fig. 4.5. We also perform computer simulations for one hundred times (which can be easily done and no bootstrap technique is required), such that there are also one hundred simulation histograms. Since there is no reason to favour a particular simulation histogram, we average these hundred histograms to obtain a single, average simulation histogram. Then, for each of the bootstrap histogram for our experimental data, we can compute its fidelity with the average simulation histogram. With hundred ensembles, we can also obtain standard deviations for the distributions of the number of witnesses needed; they will serve as the “error bars” for our histograms.

The results are shown in Fig. 4.6, where we shall focus on rank-1 and rank-2 states only, as unfortunately bootstrapping cannot be done easily due the the way we generate our rank-4 states. Reported together with the histograms are the average fidelities between the bootstrap histograms and the average simulation histograms.³

Assuming a normal distribution for large ensemble size, measure of one standard

³Note that due to non-linearity in the definition of fidelity, average of the fidelities between many distributions with a fixed reference distribution is, in general, different from the fidelity of the average distribution with the fixed reference distribution. The latter is usually larger than the former.

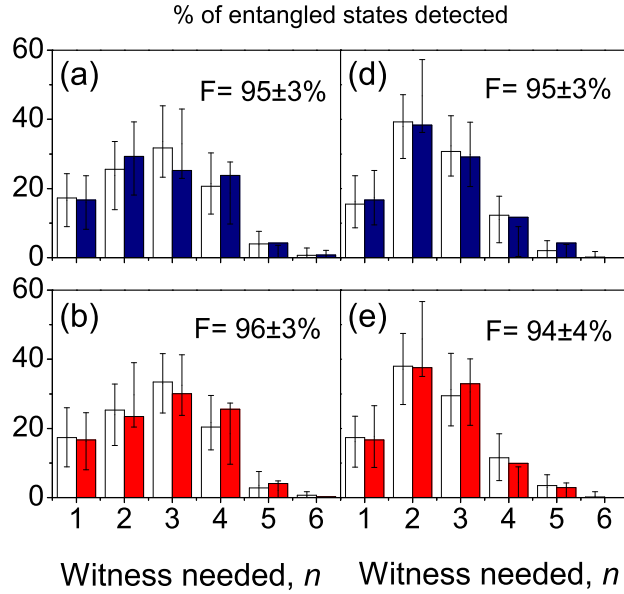


Figure 4.6: Histograms for simulated (unshaded), and experimental (shaded) results, with error bars added using the technique of bootstrapping. The first and second rows are histograms for rank-1 and rank-2 states respectively; the first and second columns are histograms for scheme B and scheme C respectively. Here, both the error bars for the simulation and bootstrap histograms are derived from 100 ensembles of about 10,000 qubit copies. The attached error bars represent one standard deviation of the number of witnesses needed. From the histograms, we see clearly that the error bars for both simulation and experimental results are very similar in size. The average fidelities are also high ($\approx 95\%$).

deviation corresponds to *confidence interval* that covers about 68% of the data. Our results show high fidelities⁴ ($\approx 95\%$) and very similar standard deviation regions for both simulations and experimental results, which again suggesting strong agreement between them. Therefore, we see that small imperfections and experimental errors negligible effects on the performance of the witness-family measurements.

Lastly, we report the average number of witnesses needed to detect entanglement. For rank-1 and rank-2 states, we summarize them in the Table 4.4 below:

For rank-4 states, the average number of witnesses needed are 2.90 (simulation) and 2.63 (experiment) for scheme B, and 2.82 (simulation) and 2.62 (experiment) for

⁴If we use fidelity between average bootstrap histograms and average simulation histograms, we will have $F \approx 99\%$

Rank & Scheme	Simulation	Experiment
1B	2.7 ± 0.3	2.6 ± 0.3
1C	2.5 ± 0.2	2.3 ± 0.2
2B	2.7 ± 0.2	2.6 ± 0.3
2C	2.5 ± 0.2	2.3 ± 0.2

Table 4.4: Average number of witnesses needed (with standard deviations) to detect entanglement for rank-1 and rank-2 states by using scheme B and scheme C respectively. In general, scheme C has a smaller mean number of witnesses needed, as well as a smaller spread.

scheme C. Of course, for all these three specific kind of states, for scheme A, the mean number of witnesses needed is 3.5. Hence, quantitatively, we have obtained consistent results that scheme C performs better than scheme B, and then scheme A.

Conclusion

In this project, the following achievements have been made:

- We have performed and realized the experiments to detect entanglement, with optimal-witness bases. In contrast to conventional witness experiments, we are measuring a family of witness at one go.
- We have introduced a novel, yet very simple method of generating mixed states by using the VPR.
- We have shown that adaptive measurement schemes allow us to reduce the mean number of witnesses needed to detect entanglement.

In summary then, we have obtained a very positive, affirmative answer to the question posted at the beginning: By measuring witness bases that form an IC POM, we can verify the presence of entanglement for a given unknown state. In fact, we have shown that by applying adaptive schemes which make use of information from each measurements, we can further reduce the number of measurements needed to obtain a conclusive identification on the separability of the given state.

Part III

Appendix

Appendix A

Witness Basis

According to the reference [LKCH00], one kind of optimal witness for bipartite systems, known as optimal decomposable witness, is given by¹

$$W = -Q^{\text{T}_2}, \quad (\text{A.1})$$

where T_2 is the partial transpose on the 2nd subsystem, and Q is a given positive operator which has no product kets in its range. Obviously, one subclass of such operator would be projectors of entangled states, $|\Psi\rangle\langle\Psi|$. In particular, for bipartite qubit, consider the kind of entangled kets parametrized by α , with $0 < \alpha \leq \pi/4$,

$$|\Psi\rangle = \cos(\alpha)|\text{VV}\rangle + \sin(\alpha)|\text{HH}\rangle. \quad (\text{A.2})$$

The partial transpose on the second qubit system for $Q = |\Psi\rangle\langle\Psi|$ is then

$$\begin{aligned} Q^{\text{T}_2} &= |\text{VV}\rangle \cos^2(\alpha) \langle\text{VV}| + |\text{HH}\rangle \sin^2(\alpha) \langle\text{HH}| \\ &\quad + |\text{VH}\rangle \sin(\alpha) \cos(\alpha) \langle\text{HV}| + |\text{HV}\rangle \sin(\alpha) \cos(\alpha) \langle\text{VH}| \\ &= |\text{VV}\rangle \cos^2(\alpha) \langle\text{VV}| + |\text{HH}\rangle \sin^2(\alpha) \langle\text{HH}| \\ &\quad + |\Phi^+\rangle \sin(\alpha) \cos(\alpha) \langle\Phi^+| - |\Phi^-\rangle \sin(\alpha) \cos(\alpha) \langle\Phi^-|. \end{aligned} \quad (\text{A.3})$$

Next, note that trace operation is not affected by partial transpose, i.e. $\text{tr}\{O\} = \text{tr}\{O^{\text{T}_2}\}$ for any operator O . In addition, taking partial transpose of a separable

¹The definition of witnesses in ref.[LKCH00] differs by a negative sign.

state results in another separable state, which is always positive. Thus,

$$\begin{aligned} \text{tr}\{\rho_{\text{sep}}W\} &= \text{tr}\{-\rho_{\text{sep}}Q^{\text{T}_2}\} = \text{tr}\{-(\rho_{\text{sep}}Q^{\text{T}_2})^{\text{T}_2}\} \\ &= \text{tr}\{-\rho_{\text{sep}}^{\text{T}_2}Q\} \leq 0, \end{aligned} \tag{A.4}$$

i.e. the witness threshold μ is 0 for this class of optimal witnesses.

Appendix B

Birefringence and Phase Matching

Before we show how one can obtain the required angle θ between optic axis (OA) and the pump's propagation \mathbf{k}_p to produce a noncollinear SPDC at desired cone-opening angle φ , see Fig. 2.1, for the sake of completeness, we need to review the subject of birefringence, in finer details than the one given in Sec. 2.2.

Birefringence

Maxwell's equations in material with no free excess charges and currents read, in cgs units,

$$\begin{aligned}\nabla \cdot \mathbf{D} &= 0, & \nabla \times \mathbf{E} &= \frac{-1}{c} \frac{\partial}{\partial t} \mathbf{B}, \\ \nabla \cdot \mathbf{B} &= 0, & \nabla \times \mathbf{H} &= \frac{1}{c} \frac{\partial}{\partial t} \mathbf{D}.\end{aligned}\tag{B.1}$$

For linear dielectric material which is magnetically not active, the magnetic induction $\mathbf{H}(\mathbf{r}, t)$ equals the magnetic field $\mathbf{B}(\mathbf{r}, t)$, and the displacement vector $\mathbf{D}(\mathbf{r}, t)$ is linearly related to the electric field $\mathbf{E}(\mathbf{r}, t)$, through $\mathbf{D}(\mathbf{r}, t) = \overleftrightarrow{\epsilon} \cdot \mathbf{E}(\mathbf{r}, t)$. Here, $\overleftrightarrow{\epsilon}$ is known as the *dielectric tensor*; the material is said to be *anisotropic* when it is not proportional to the identity tensor. In particular, consider plane monochromatic electromagnetic (EM) waves of wave vector \mathbf{k} and angular frequency ω propagating in the material, i.e. $\mathbf{E}(\mathbf{r}, t) = \mathbf{E}_0 e^{-i(\omega t - \mathbf{k} \cdot \mathbf{r})}$. The two inhomogeneous Maxwell's

equations then give

$$\frac{\omega}{c}\mathbf{H} = \mathbf{k} \times \mathbf{E}, \quad \frac{\omega}{c}\mathbf{D} = -\mathbf{k} \times \mathbf{H}. \quad (\text{B.2})$$

Define $\mathbf{n} = \frac{c}{\omega}\mathbf{k}$, so that $|\mathbf{n}|$ is the refractive index $n = c/v$, where v is the speed of light in the material, and using $\mathbf{D}(\mathbf{r}, t) = \overleftrightarrow{\epsilon} \cdot \mathbf{E}(\mathbf{r}, t)$, Eqs. (B.2) give

$$\mathbf{D} = -\mathbf{n}(\mathbf{n} \cdot \mathbf{E}) + n^2 \mathbf{E}, \quad (\text{B.3})$$

$$\text{or } D_i = (n^2 \delta_{ik} - n_i n_k) E_k = \epsilon_{ik} E_k, \quad (\text{B.4})$$

which shows that for unique and nontrivial solution for \mathbf{E} , we have

$$\det |n^2 \delta_{ik} - n_i n_k - \epsilon_{ik}| = 0. \quad (\text{B.5})$$

Except for exoctic material like gyrotropic media which we shall not consider, the dielectric tensor is symmetric, and hence diagonalizable in certain unit basis, which we shall call the *principle axes* $\{\mathbf{e}_x, \mathbf{e}_y, \mathbf{e}_z\}$. Evaluate the determinant in this basis, one gets

$$n^2(\epsilon_x n_x^2 + \epsilon_y n_y^2 + \epsilon_z n_z^2) - \left[n_x^2 \epsilon_x (\epsilon_y + \epsilon_z) + n_y^2 \epsilon_y (\epsilon_x + \epsilon_z) + n_z^2 \epsilon_z (\epsilon_x + \epsilon_y) \right] + \epsilon_x \epsilon_y \epsilon_z = 0. \quad (\text{B.6})$$

This is known as the *Fresnel's equation*, one of the fundamental equations in crystal optics. For *uniaxial* crystals, where $\epsilon_x = \epsilon_y \equiv \epsilon_\perp$ and $\epsilon_z \equiv \epsilon_\parallel$ without loss of generality, the Fresnel's equation reads

$$(n^2 - \epsilon_\perp) \left(\epsilon_\parallel n_z^2 + \epsilon_\perp (n_x^2 + n_y^2) - \epsilon_\perp \epsilon_\parallel \right) = 0, \quad (\text{B.7})$$

and the solutions are therefore

$$n^2 = \epsilon_\perp, \quad (\text{B.8})$$

$$\frac{n_z^2}{\epsilon_\perp} + \frac{n_x^2 + n_y^2}{\epsilon_\parallel} = 1. \quad (\text{B.9})$$

The principle axis that has different dielectric constant than the others is known as the *optic axis* (OA), and if $\epsilon_{\perp} > \epsilon_{\parallel}$, we have a *negative* crystal, as opposed to otherwise a *positive* crystal. The two solutions imply two possible ways of propagation of light in the crystal. One of them is known as the *ordinary ray*, propagating with constant speed determined by $n = \sqrt{\epsilon_{\perp}} \equiv n_o$. Denoting θ as the angle between OA and \mathbf{n} , the second ray, known as the *extraordinary ray*, propagates at speed determined by the equation

$$\frac{\cos^2(\theta)}{\epsilon_{\perp}} + \frac{\sin^2(\theta)}{\epsilon_{\parallel}} = \frac{1}{n^2} \equiv \frac{1}{n_e^2(\theta)}. \quad (\text{B.10})$$

Polarization of the rays

To investigate the polarizations, i.e. the directions of \mathbf{D} of the ordinary and extraordinary rays in such uniaxial crystal, consider first the energy density stored in the electric field, i.e.

$$\begin{aligned} u &= \frac{1}{8\pi} \mathbf{E} \cdot \mathbf{D} = \frac{1}{8\pi} \sum_{k,l} E_k \epsilon_{kl} E_l \\ &= \frac{1}{8\pi} \left(\frac{D_x^2 + D_y^2}{\epsilon_{\perp}} + \frac{D_z^2}{\epsilon_{\parallel}} \right), \end{aligned} \quad (\text{B.11})$$

expressed once again in the principle axes. Since u is positive, Eq.(B.11) is geometrically an ellipsoid equation. Also, since \mathbf{D} and \mathbf{k} are mutually perpendicular, the possible directions for \mathbf{D} are further restricted to an ellipse, obtained as the boundary of the cross section of the ellipsoid, cut through the origin and is normal to the \mathbf{k} . Now, since we have either ordinary or extraordinary ray, we anticipate that the \mathbf{D} are further restricted to two points on the ellipse¹. Introducing a unit basis $\{\mathbf{e}_{\alpha}, \mathbf{e}_{\beta}, \mathbf{e}_{\gamma}\}$ where $\mathbf{k} = |\mathbf{k}| \mathbf{e}_{\gamma}$, we have $D_{\alpha} = \epsilon_{\alpha\beta} E_{\beta}$ or $E_{\alpha} = (\epsilon^{-1})_{\alpha\beta} D_{\beta}$ and $\mathbf{n} = n_{\gamma} \mathbf{e}_{\gamma}$, Eq. (B.3) reads

$$\left(\frac{1}{n^2} \delta_{\alpha\beta} - (\epsilon^{-1})_{\alpha\beta} \right) D_{\beta} = 0, \quad (\text{B.12})$$

¹More rigorously, one can show that Eq.(B.11) and $\mathbf{D} \cdot \mathbf{k} = 0$, subjected to the constraint Eq. (B.3) from Maxwell's equation, is equivalent to finding the points of extremum distance on the ellipse from the origin, which admits two solutions. They are the semiminor and semimajor axes, of course.

which can be further diagonalized such that

$$\begin{pmatrix} \frac{1}{n^2} - \epsilon_i^{-1} & 0 \\ 0 & \frac{1}{n^2} - \epsilon_j^{-1} \end{pmatrix} \begin{pmatrix} D_i \\ D_j \end{pmatrix} = 0. \quad (\text{B.13})$$

\mathbf{D} being nonzero requires $\epsilon_i^{-1} = 1/(n_o^2)$ and $\epsilon_j^{-1} = 1/(n_e^2)$ for instance, which in return requires the polarizations of ordinary and extraordinary rays to be perpendicular.

Finally, we can see that the only consistent \mathbf{D} are the semiminor and semimajor axes of the ellipse. The semiminor axis corresponds to the polarization of ordinary ray, since when $\theta \rightarrow 0$ in Eq. (B.10), $n_e(\theta \rightarrow 0) \rightarrow n_o$, while the ellipse of \mathbf{D} becomes a circle. Though the \mathbf{D} can have infinitely many possibilities now, they are essentially perpendicular to OA and \mathbf{k} . Since in principle one has no right to argue if a light propagating with $n = n_o$ is in principle a ‘real’ ordinary ray or ‘had originated from an extraordinary ray with $\theta \rightarrow 0$ ’, all ordinary rays must be perpendicular to the plane of OA and \mathbf{k} . For \mathbf{k} not collinear with OA, this is the semiminor axis of the ellipse. For extraordinary ray, it is the semimajor axis, which is coplanar with OA and \mathbf{k} .

Phase matching for SPDC

In real experiment, pre-design of the set-up is crucial, such as to reduce the cost, or to meet the requirement from a limited lab space. Suppose by using a pump laser of wavelength 404.6 nm, we wish to obtain noncollinear degenerate SPDC with a cone-opening angle φ of about 4° , see Fig. 2.1 for illustration. Setting this as a constraint, we would like to obtain the phase-matching angle θ .

First, we determine the angle $\vartheta/2$, by the Snell’s law:

$$n_o(809.12 \text{ nm}) \sin\left(\frac{\vartheta}{2}\right) = \sin(4^\circ). \quad (\text{B.14})$$

Note that n for both ordinary and extraordinary rays are usually decreasing functions of wavelength, i.e. $n(404.6 \text{ nm}) > n(809.12 \text{ nm})$ due to dispersive property of the crystal. In general, for each wavelength λ , the values of ϵ_\perp and ϵ_\parallel character-

izing the material are different. After much effort from the community, they can be summarized in the *empirical Sellmeier formula* [DGN99]: for BBO crystals, it reads

$$\epsilon_{\perp}(\lambda) = 2.7359 + \frac{0.01878}{\lambda^2 - 0.01822} - 0.01354\lambda^2, \quad (\text{B.15})$$

$$\epsilon_{\parallel}(\lambda) = 2.7353 + \frac{0.01224}{\lambda^2 - 0.01667} - 0.01516\lambda^2, \quad (\text{B.16})$$

where λ is in unit of μm . Since we are targeting Type-I phase matching with ‘e \rightarrow o + o’ configuration, we are looking for

$$\begin{aligned} \epsilon_{\perp}(809.2 \text{ nm}) &= 2.75654, \\ \epsilon_{\perp}(404.6 \text{ nm}) &= 2.86277, \\ \epsilon_{\parallel}(404.6 \text{ nm}) &= 2.45607. \end{aligned} \quad (\text{B.17})$$

Equation (B.14) then gives

$$\frac{\vartheta}{2} = \arcsin\left(\frac{\sin(4^\circ)}{\sqrt{2.75654}}\right) = 2.408^\circ. \quad (\text{B.18})$$

Lastly, we obtained the required $n_e(404.6 \text{ nm}, \theta)$ by Eq. (2.12), i.e.

$$n_e^2(404.6 \text{ nm}, \theta) = 2.75654 \cos^2(2.408^\circ) = 2.75167 \quad (\text{B.19})$$

and solve Eq. (B.10) inversely, giving us $\theta = 29.59^\circ$. This agrees very well with the results obtained from *NIST Phasematch* programme.

An important remark on the technical side of the experiment is this: Should we have chosen the cone-opening angle to be $\varphi = 3^\circ$, the phase-matching angle needed would have been $\theta = 29.26^\circ$. Since 29.26° is relatively close to 29.59° , this shows that by turning the pitch of the platform where the crystal is mounted on (assuming a vertically polarized pump), there are flexibilities in tuning the cone-opening angle. Usually, such standard platform (e.g. KM100PM, Thorlabs) allows adjustment of about $\pm 3^\circ$ for both the yaw and pitch degrees of freedom, which allows θ to vary from about 26.6° to 32.6° , corresponds to cone-opening angle from 0° to about 9.10° .

Appendix C

Coherence Length and the Migdall Effect

In this appendix, we discuss two issues that we faced in controlling the quality of our photonic systems. They are: the coherence length of the pump laser, and the so-called Migdall effect [Mig97, RUK11] on the polarization of the down-converted photons.

Coherence length

The (longitudinal or temporal) *coherence length* of a laser measures its degree of phase stability or phase coherence [MW95]. In essence, for a given coherence length L_c , the phase of the light within spatial intervals of L_c will be strongly correlated. Another quantity of same physical significance is the *coherence time* τ_c , which is given by L_c/c , where c is the speed of light.

The coherence time of a light is inversely proportional to its effective spectral width or bandwidth $\Delta\nu$, where the proportional factor depends on the definition of the bandwidth [MW95, ST91]. Usually, $\Delta\nu \cdot \tau_c$ is about from 0.1 to 1. As commented in the reference [MW95], “different definitions may lead to results of quite different orders of magnitude ... caution must be exercised ...”.

When our pump laser was first bought, the specification sheet from the company states that the bandwidth is about 160 MHz. Using $\Delta\nu \cdot \tau_c = 1$, we then have

$L_c \approx 1.87$ m. As this value is much larger than the thickness of our crystals, the phase of the pump across them will be strongly correlated, and Eq. (3.1) is applicable. As a careful measure, we also determine the bandwidth of the laser with our own optical spectrum analyzer (Ando/Yokogawa AQ-series), which has a resolution limit of 0.05 nm (wavelength). A frequency bandwidth of $\Delta\nu$ is equivalent to having $\Delta\lambda = (c\Delta\nu)/\nu^2$, in terms of wavelength bandwidth. Then, one has the relationship $L_c \approx \lambda^2/\Delta\lambda$. The result from our spectrum analyzer was in agreement with the manufacturer's report: For $\Delta\nu = 160$ MHz, $\Delta\lambda = 8.7 \times 10^{-14}$ m, we obtained the resolution limit for our spectrum analyzer, indeed.

Unfortunately, the laser broke down just not too long before the project was starting for serious. The visibility of polarization correlation analysis for the supposedly Bell state was dropped to about 92%. We then re-checked the bandwidth of the pump laser by using the spectrum analyzer and found that it had increased to about 0.1 nm to 0.3 nm (which corresponds to $L_c \approx 0.5$ mm), and was unstable throughout the day.

The laser was then sent for repair, where the manufacturer inspected that “the output of the diode is damaged . . . there are additional structures that is not typical of our diodes in the output beam . . . the power has dropped to 17 mW”. The repair cost us about SGD1000, and the newly reported bandwidth from the manufacturer is $\Delta\lambda \approx 0.037$ nm. This corresponds to $L_c \approx 4$ mm.

However, by using our own spectrum analyzer, we found disagreement with the reported values from the manufacturer, as we obtained a value of about 0.12 nm instead. The issue was raised to the manufacturer, who replied “. . . we have these instruments as well and we never measure the linewidth to be at the resolution limit of the instrument . . . using a higher resolution (0.020 nm) Yokogawa, the diode was measured to the attached test report [0.037 nm]”. Also, taking into account different possible definitions of the bandwidth and coherence length, a definite value for the coherence length was then never exactly pinpointed.

We settle this issue of uncertainty in coherence length with the *experimental observations* that high visibilities of the polarization correlation analysis, using the Bell states, were consistently obtained thereafter, see Sec. 3.3.2. In addition, high

fidelties of the produced states, see Sec. 4.1, also convinced us that we are in the safe region where the coherence length is indeed long enough to make sure that Eq. (3.1) is satisfied. With this, we can put aside this issue of coherence length in this project, at least to first order.

Migdall effect

First, recall that for Type-I phase matching or ‘e \rightarrow o + o’ configuration, the pump laser will experience extraordinary refractive index, while the signal and idler photons will experience ordinary refractive index, inside the negative crystal. In particular, we are only interested in the situation where the propagation or wave vectors of the down-converted photons and the pump are all contained in the same plane parallel to the table surface, which we shall now call as the x - y plane.

Then, there are two particular cases. One is when the polarization of the pump and the optic axis of the crystal are both contained in this x - y plane as well. Furthermore, let the wave vector of the pump be along the x -axis. This results in the polarization of the down-converted photons being perpendicular to the x - y plane, which we shall call as the z -axis; see Fig. 2.1 for the illustration. Obviously, this corresponds to the generation of $|v\rangle$ ket in our two-type I crystal geometry, after we recognize the x - y plane as the plane that defines horizontal polarization, and z -axis as the vertical direction.

There is another situation, which corresponds to the generation of $|H\rangle$ ket from the second crystal. Here, the polarization of the pump is along the z -axis, and the crystal optic axis (OA) is in the x - z plane. Since the polarization of the down-converted photons must be perpendicular to the OA, it turns out that it cannot be contained in the x - y plane, and hence the ket generated is actually *not* exactly $|H\rangle$. To obtain a quantitative measure about this discrepancy, consider the cone-opening angle to be 3° , and the angle between OA and the pump’s wave vector to be 29.5° .

Then, in the Cartesian coordinates, we have

$$\mathbf{OA} \hat{=} \begin{pmatrix} \cos(29.5^\circ) \\ 0 \\ \sin(29.5^\circ) \end{pmatrix} \quad ; \quad \mathbf{k}_s \hat{=} \begin{pmatrix} \cos(2.408^\circ) \\ \sin(2.408^\circ) \\ 0 \end{pmatrix}, \quad (\text{C.1})$$

and the vector that is perpendicular to both is given by

$$\mathbf{J} \equiv \mathbf{k}_s \times \mathbf{OA} \hat{=} \begin{pmatrix} \sin(2.408^\circ) \sin(29.5^\circ) \\ -\cos(2.408^\circ) \sin(29.5^\circ) \\ \sin(2.408^\circ) \cos(29.5^\circ) \end{pmatrix}. \quad (\text{C.2})$$

Compare this with the horizontal polarization $|\text{H}\rangle$ which is represented by

$$\mathbf{H} \hat{=} \begin{pmatrix} \cos(2.408^\circ) \\ \sin(2.408^\circ) \\ 0 \end{pmatrix} \times \begin{pmatrix} 0 \\ 0 \\ 1 \end{pmatrix} = \begin{pmatrix} \sin(2.408^\circ) \\ -\cos(2.408^\circ) \\ 0 \end{pmatrix} \quad (\text{C.3})$$

such that $\mathbf{J} \cdot \mathbf{H} = |\mathbf{J}| \cos(\gamma)$, we find that the two vectors differ by $\gamma \approx 4.3^\circ$. This value can also be obtained using a more general method considered in the reference [Mig97, RUK11].

The fidelity between the kets of $|4.3_s 4.3_i\rangle$ and the $|\text{HH}\rangle$ is $(\cos(4.3^\circ))^2 \approx 99.4\%$, which shows that inasmuch there is a intrinsic error in our generation of the photon states, the errors are relatively small and can be ignored, to the first order approximation. Of course, the value $F = 99.4\%$ will remind us about the limit of our experimental precision; see Sec. 4.1 for the results. Unfortunately, due to limitation of lab space, one hardly can reduce the cone-opening angle to smaller than 3° .

Appendix D

SPDC Coupling and Polarization Control

In the first part of this appendix, we explain why we put our lenses at about one meter away from the crystals. In the second section, we discuss how to use the manual polarization controllers to neutralize any unwanted polarization changes due to fibers and any other optical component.

SPDC coupling

To collect the SPDC light as efficient as possible, the frequency spectrum of the SPDC is first to be estimated. This can be obtained conveniently by utilizing the *NIST Phasematch* software mentioned in Sec. 2.2, see Fig. 2.2. In particular, we will pay concern to wavelengths range in between 810 ± 10 nm, in accordance with the specifications of our interference filters. This corresponds to spatial angles $\Delta\theta \approx 4.10^\circ - 3.95^\circ = 0.15^\circ \approx 0.0026$ rad¹.

On the other hand, any optical fiber has its *numerical aperture* (NA), which can be approximated as its maximum acceptance angle. For single-mode fibers that we are using, their NAs are about 0.12. Hence, to couple in as much as possible the down-converted photons, by putting the single-mode fiber tip at the focus of the lens, the approximate optimal distance, d , measured from the SPDC source to the

¹We used cone-opening angle of 3° instead 4° in our experiment, but no significant deviation is expected.

lens with focus f is given by, see Fig. D.1 for illustration,

$$d \approx \frac{0.12}{0.0013} f \approx 92. \quad (\text{D.1})$$

For $f = 11 \text{ mm}$, we have $d \approx 1 \text{ m}$.

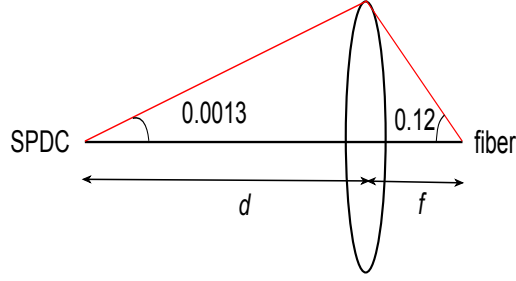


Figure D.1: Illustration of how the lens captures the SPDC photons at d distance away, and couples them into the single mode with $\text{NA}=0.12$, located at its focus.

Polarization control

To make sure that all the unintended polarization changes due to the optical fibers, and possibly mirrors and other optical components are compensated for, manual polarization controllers are used. To do this, a light source from an auxiliary laser of wavelength 810 nm is coupled into the single-mode fiber, through the lens that collect the signal or idler photons. Just before the two mirrors in front of the lens, see Fig. 3.1, a PBS is inserted, so that the input light is characterized by $|H\rangle$. A second, and analyzing PBS is then inserted just before the BS used for the HOM interference, with a power meter recording the intensity at the reflection output port, i.e. the vertical component of the output light.

To neutralize any unwanted polarization changes, the paddles of the polarization controllers are turned such that the power meter registers a minimum value. This corresponds to having a channel with the operation $|H\rangle \rightarrow e^{i\phi_1}|H\rangle$, $|V\rangle \rightarrow e^{i\phi_2}|V\rangle$, with ϕ_1 not necessarily equals ϕ_2 . To make sure that ϕ_1 equal to ϕ_2 , the input light is set at 45° polarization with help of a HWP. Another HWP is also inserted in front of the analyzing PBS such that the power meter now measures the intensity of -45° polarization component. ϕ_1 and ϕ_2 are concluded to be equal, and hence a identity or polarization preserving channel is established from the source of SPDC

to just before the BS, when the power meter registers minima intensities in both measurement bases. In our experiments, the *suppression ratios*, i.e. the ratios of intensities at between the transmission and the reflection output port of the analyzing PBS, are obtained to be about 70 for both bases.

Bibliography

- [AGR81] A. Aspect, P. Grangier, and G. Roger. Experimental tests of realistic local theories via Bell's theorem. *Physical Review Letters*, 47:460–463, 1981.
- [BDSW96] C. H. Bennett, D. P. DiVincenzo, J. A. Smolin, and W. K. Wootters. Mixed-state entanglement and quantum error correction. *Physical Review A*, 54(5):3824, 1996.
- [Blo96] N. Bloembergen. *Nonlinear Optics*. World Scientific, 1996.
- [Boh28] N Bohr. The quantum postulate and the recent development of atomic theory. *Nature*, 121:580–590, 1928.
- [BPM⁺97] D. Bouwmeester, J.-W. Pan, K. Mattle, M. Eibl, H. Weinfurter, and A. Zeilinger. Experimental quantum teleportation. *Nature*, 390(6660):575–579, 1997.
- [BW99] M. Born and E. Wolf. *Principles of Optics*. Cambridge University Press, 1999.
- [BŻ06] I. Bengtsson and K. Życzkowski. *Geometry of Quantum States: An Introduction to Quantum Entanglement*. Cambridge University Press, 2006.
- [CG04] D. Collins and N. Gisin. A relevant two qubit Bell inequality inequivalent to the CHSH inequality. *Journal of Physics A: Mathematical and General*, 37(5):1775, 2004.

- [Che99] M. R. Chernick. *Bootstrap methods: A guide practitioner's guide*. Wiley, 1999.
- [CKW00] V. Coffman, J. Kundu, and W. K. Wootters. Distributed entanglement. *Physical Review A*, 61:052306, 2000.
- [CS78] J. F. Clauser and A. Shimony. Bell's theorem. Experimental tests and implications. *Reports on Progress in Physics*, 41(12):1881, 1978.
- [Dav97] A. C. Davison. *Bootstrap methods and their application*. Cambridge University Press, 1997.
- [DGN99] V. G. Dmitriev, G. G. Gurzadyan, and D. N. Nikogosyan. *Handbook of Nonlinear Optical Crystals*. Springer, 1999.
- [DLT⁺13] J. Dai, Y. L. Len, Y. S. Teo, L. A. Krivitsky, and B.-G. Englert. Controllable generation of mixed two-photon states. *New Journal of Physics*, 15(6):063011, 2013.
- [Eke91] A. K. Ekert. Quantum cryptography based on Bell's theorem. *Physical Review Letters*, 67:661–663, 1991.
- [EKW01] B.-G. Englert, C. Kurtsiefer, and H. Weinfurter. Universal unitary gate for single-photon two-qubit states. *Physical Review A*, 63(3):032303, 2001.
- [Eng96] B.-G. Englert. Fringe visibility and which-way information: An inequality. *Physical Review Letters*, 77:2154–2157, 1996.
- [Fis22] R. A. Fisher. On the mathematical foundations of theoretical statistics. *Philosophical Transactions of the Royal Society of London. Series A, Containing Papers of a Mathematical or Physical Character*, 222:309–368, 1922.
- [Hay06] M. Hayashi. *Quantum Information: An Introduction*. Springer, 2006.
- [Hel76] C. W. Helstrom. *Quantum Detection and Estimation Theory*. Academic Press, 1976.

- [HHH96] M. Horodecki, P. Horodecki, and R. Horodecki. Separability of mixed states: necessary and sufficient conditions. *Physics Letters A*, 223(1):1–8, 1996.
- [HM84] M. Hillery and L. D Mlodinow. Quantization of electrodynamics in nonlinear dielectric media. *Physical Review A*, 30(4):1860, 1984.
- [HOM87] C. K. Hong, Z. Y. Ou, and L. Mandel. Measurement of subpicosecond time intervals between two photons by interference. *Physical Review Letters*, 59:2044–2046, 1987.
- [Joz94] R. Jozsa. Fidelity for mixed quantum states. *Journal of Modern Optics*, 41(12):2315–2323, 1994.
- [KW98] P. G. Kwiat and H. Weinfurter. Embedded Bell-state analysis. *Physical Review A*, 58(4):R2623–R2626, 1998.
- [KWW⁺99] P. G. Kwiat, E. Waks, A. G. White, I. Appelbaum, and P. H. Eberhard. Ultrabright source of polarization-entangled photons. *Physical Review A*, 60(2):773–776, 1999.
- [Lan98] L. D. Landau. *Electrodynamics of Continuous Media: Landau and Lifshitz Course of Theoretical Physics, vol. 8*. Pergamon Press, Oxford, 1998.
- [LHLLK06] A. Ling, P. Y. Han, A. Lamas-Linares, and C. Kurtsiefer. Preparation of Bell states with controlled white noise. *Laser Physics*, 16(7):1140–1144, 2006.
- [LKCH00] M. Lewenstein, B. Kraus, J. I. Cirac, and P. Horodecki. Optimization of entanglement witnesses. *Physical Review A*, 62(5):052310, 2000.
- [Mig97] A. Migdall. Polarization directions of noncollinear phase-matched optical parametric downconversion output. *Journal of the Optical Society of America B*, 14(5):1093–1098, 1997.
- [MW95] L. Mandel and E. Wolf. *Optical Coherence and Quantum Optics*. Cambridge University Press, 1995.

- [NC10] M. A. Nielsen and I. L. Chuang. *Quantum Computation and Quantum Information*. Cambridge University Press, 2010.
- [Per95] A. Peres. *Quantum Theory: Concepts and Methods*. Springer, 1995.
- [PR04] M. Paris and J. Reháček. *Quantum State Estimation*. Springer, 2004.
- [ŘHKL07] J. Řeháček, Z. Hradil, E. Knill, and A. I. Lvovsky. Diluted maximum-likelihood algorithm for quantum tomography. *Physical Review A*, 75(4):042108, 2007.
- [RUK11] R. Rangarajan, A. B. U'Ren, and P. G. Kwiat. Polarization dependence on downconversion emission angle: investigation of the ‘Migdall effect’. *Journal of Modern Optics*, 58(3-4):312–317, 2011.
- [Sch60] Julian Schwinger. Unitary operator bases. *Proceedings of the national academy of sciences of the United States Of America*, 46(4):570, 1960.
- [Sch00] J. Schwinger. *Quantum Kinematics and Dynamics*. Westview Press, 2000.
- [Sch01] J. Schwinger. *Quantum Mechanics. Symbolism of Atomic Measurements*. Berlin: Springer, 2001.
- [ST91] B. E. A. Saleh and M. C. Teich. *Fundamentals of Photonics*. Wiley New York, 1991.
- [Teo13] Y. S. Teo. Numerical estimation schemes for quantum tomography. *arXiv preprint arXiv:1302.3399*, 2013.
- [Ter00] B. M. Terhal. Bell inequalities and the separability criterion. *Physics Letters A*, 271(5):319–326, 2000.
- [TSE⁺12] Y. S. Teo, B. Stoklasa, B.-G. Englert, J. Reháček, and Z. Hradil. Incomplete quantum state estimation: A comprehensive study. *Physical Review A*, 85(4):42317, 2012.
- [TZE⁺11] Y. S. Teo, H. Zhu, B.-G. Englert, J. Řeháček, and Z. Hradil. Quantum-state reconstruction by maximizing likelihood and entropy. *Physical Review Letters*, 107(2):020404, 2011.

-
- [Wer89] R. F. Werner. Quantum states with Einstein-Podolsky-Rosen correlations admitting a hidden-variable model. *Physical Review A*, 40:4277–4281, 1989.
- [Woo98] W. K. Wootters. Entanglement of formation of an arbitrary state of two qubits. *Physical Review Letters*, 80:2245–2248, 1998.
- [ZTE10] H. Zhu, Y. S. Teo, and B.-G. Englert. Minimal tomography with entanglement witnesses. *Physical Review A*, 81(5):052339, 2010.

